ABSTRACT

Title of dissertation: METHODS FOR CHARACTERIZING ELECTROMAGNETIC COUPLING STATISTICS IN COMPLEX ENCLOSURES

Bisrat Demeke Addissie
Doctor of Philosophy, 2017

Dissertation directed by: Professor Thomas Antonsen
Department of Electrical and Computer Engineering

The random coupling model (RCM) can be used to characterize the electromagnetic coupling between multiple ports inside large complex enclosures. This statistical model combines nonrandom parameters of the enclosure and ports with a universally distributed random variable. A strong appeal of the RCM is the ability to characterize a wide variety of enclosure configurations with a limited number of parameters. However, in practical enclosures, these parameters can be difficult to obtain. In the first part of dissertation, nonintrusive measurement methods are developed that use the time gating technique to acquire the nonrandom system parameters. Additionally, a problematic case of high loss antenna in enclosures is addressed. For the high loss antenna case, the radiation impedance is very difficult to obtain and difficult to use if obtained. For this reason, a modified random coupling model is formulated to make use of the radiation efficiency of the antennas. These methods have been successfully tested in multiple enclosures and ports. In the second part of the dissertation, the limitation of applicability of the RCM at

lower frequencies is explored. The RCM assumes an overmoded cavity and that the random plane wave hypothesis applies. The breakdown of these assumptions is measured at lower frequencies and metrics are developed to determine the lowest usable frequency of the RCM. Lastly, the concepts of the RCM and the tools of microwave systems are used to experimentally validate the theory of regularization of quantum tunneling rates in chaotic cavities. The theory is based on the random plane wave hypothesis and can be studied in microwave cavities. The theory and the validating experiments are presented.

METHODS FOR CHARACTERIZING ELECTROMAGNETIC COUPLING STATISTICS IN COMPLEX ENCLOSURES

by

Bisrat Demeke Addissie

Dissertation submitted to the Faculty of the Graduate School of the
University of Maryland, College Park in partial fulfillment
of the requirements for the degree of
Doctor of Philosophy
2017

Advisory Committee:
Professor Thomas Antonsen, Chair/Advisor
Professor Edward Ott
Professor Mario Dagenais
Dr. John Rodgers
Professor Steven Anlage

Dedication

To my parents Amsale Bogale and Demeke Addissie Babu.

Acknowledgments

The work in this dissertation was funded by Office of Naval Research under grant N00014130474 and and the Air Force Office of Scientific Research Center of Excellence under grant FA9550-15-1-0171. I would like to thank both organizations for funding my research.

I would like to thank my advisor Professor Antonsen for his unwavering support and encouragement throughout my PhD program. I could always count on him to give me a sense of direction during the difficult times. I also like to thank Dr. John Rodgers who has advised me from my time as an undergraduate student. I will always be thankful to him for convincing me to pursue my PhD. I would also like to thank Professor Anlage and Professor Ott for providing constant feedback and useful suggestions throughout my PhD research. Our discussions in the Wave Chaos group meetings were very helpful. I thank the student members of the Wave Chaos group as well for their feedback and support. Finally, I thank Professor Dagenais for agreeing to serve on dissertation defense committee. Thank you all!

Table of Contents

List of Figures

Chapter 1: Introduction

1.1 Motivation

Understanding wave propagation in geometrically irregular regions is a common challenge in science and engineering. The waves of interest may be classical electromagnetic waves [1, 2], quantum mechanical waves [3, 4], or acoustic waves [5–7]. In the case of acoustic waves, the interest is the distribution of the sound in a reverberant environment. A loud bang on one point inside an irregular enclosure, such as submarine, can produce locations of very high peaks of sound energy due to interference pattern within the enclosure. This is of great interest to designing such enclosures. The nature of short wavelength electromagnetic radiation inside complex enclosures is of interest to the electromagnetic compatibility (EMC) community, which studies the possibility of radiation from an electromagnetic source coupling EM energy to other sensitive electronics [8]. This has become increasingly important with the prevalence of electronic devices in enclosures and sources of EM radiation [9]. Predictive models for the induced voltages and currents in these devices are necessary to determine the potential for damage. The work in this dissertation is aimed at improving the analytical models used to predict coupling in reverberant enclosures. The types of enclosures for which the research in this

dissertation is relevant include computer boxes, submarines, and avionics bay of aircrafts, etc.

Any model used to characterize coupling in these enclosures must describe two types of ports. One type of port is an antenna intended to couple EM into the enclosures. A second type of port is an unintended port such as small openings in the enclosure as well as exposed cables that, while are not designed to couple EM radiation, but do so anyway. The latter is often of bigger concern because the devices exposed to the EM radiation through unintended ports are not properly shielded.

In order to characterize the coupling of electromagnetic energy, a deterministic approach may seem appropriate, but there are several reasons a statistical approach is preferred. For most irregular geometries, an analytical solution does not exist. However, numerical algorithms are available in commercial software to deterministically solve for the electromagnetic fields inside the enclosures. The EM fields will depend of the geometry, the material properties of the enclosure and the frequency of excitation. In the small wavelength limit, where the ratio of the enclosure dimensions to the wavelength is large, the numerical solver must mesh the geometry covering it with a very large number of grid points. Even with the advancement of modern computers, the amount of memory and computational power required to numerically solve the problem can become impractical. In addition to this, the nature of the waves in the complex enclosure is such that small changes to the boundary conditions or the frequency dramatically change the wave dynamics, changing the solution substantially. Moreover, any inaccuracy in modeling the material or the ge-

ometry, will also lead to incorrect solutions. For these reasons, researchers studying EM energy in complex enclosures have found it more useful to study the statistical wave properties.

Random matrix theory (RMT), which is discussed in the next section, has been a successful tool to describe the statistics of eigenvalues of the wave equation for irregular enclosures in the small wavelength limit. However, in practical systems, the results from RMT need to be combined with unique port characteristics to form a complete statistical model of a multi-port enclosure. The Random Coupling Model (RCM), developed at the University of Maryland is such a model. It has been studied theoretically [10,11] and validated experimentally [12]. The RCM is a focus point for the dissertation, but there are similar models in the literature such as one by L.K. Warne et. al at Sandia National Laboratory [13] for which the work in this dissertation is applicable. The primary motivation of the work in this dissertation is to establish methods to retrieve the important "system specific" information of practical systems, so that the model is useful in characterizing coupling statistics.

1.2 History

Much of the work in the EMC community involves ad hoc measurements of EM fields in reverberation chambers. The measured fields are highly sensitive to small changes in the orientation or location of the source, and the frequency of excitation. However, the probability distributions of the field amplitudes are known to be much less sensitive and can even be universal. Price et. al [2] were the first to ?characterize

the distributions of the field amplitude. They claimed that it has a "universal" distribution that is a function of less sensitive parameters such as the number of modes simultaneously excited in the cavity. Others have subsequently studied this phenomenon [14, 15]. The reason behind this universal distribution is addressed by the University of Maryland wave chaos research group in the development of random coupling model.

The random coupling model is rooted in the original work by Eugene P. Wigner [16]. He was interested in the statistics of the energy levels of large nuclei. He found that the probability distribution of the spacing between energy levels is the same as the spacing between an eigenvalues of a random matrix with particular properties. Two of the random matricies Wigner discusses are important for the RCM, the Gaussian orthogonal ensemble (GOE) and the Gaussian unitary ensemble (GUE). Each of which are applicable to different systems as described later in this section. The elements of the matrices are independent Gaussian random variables with zero mean. The elements of the GOE matricies are real with different variances for the diagonal and off-diagonal elements. The main property of GOE matrices is invariance under orthogonal transformation. That is, the probability distribution of an ensemble of matrices has the property that $P(H) = P(OHO^T)$ where O is an arbitrary orthogonal matrix and the O^T is its transpose. On the other hand, the GUE matrices have elements of complex numbers, and the matrices are invariant under unitary transformation such that $P(H) = P(UHU^\dagger)$ where U is arbitrary unitary matrix and $U^\dagger$ is its conjugate traspose.

Others have shown that Wigner's random matrices can be applied to find

the distributions of the resonant frequencies in a variety of wave systems including complex electromagnetic enclosures [17,18]. A key quantity addressed is the spacing between nearest neighbor frequencies of resonant modes (or energies in the case of nuclei). The distribution of the spacing has universal properties that we exploit to statistically characterize our systems. In the case of electromagnetic enclosures, we focus on spacing between the resonant wavenumbers squared, k_n^2, where $\omega_n = k_n c$ is the resonant frequency. The mean mode spacing ($\Delta k^2 = \langle k_{n+1}^2 - k_n^2 \rangle$) can be approximated by Weyl's formula. For 3D electromagnetic enclosures, it is given by $\Delta k^2 = 2\pi^2/kV$, where $k = \omega/c$ and V is the volume of the enclosure [19]. Thus, we consider the distribution of

$$s = \frac{k_{n+1}^2 - k_n^2}{\Delta k^2}. \tag{1.1}$$

In the case where the system has time reversal symmetry, the probability distribution of s takes the form [17].

$$P_{GOE}(s) \cong \frac{\pi}{2} s e^{-\pi s^2/4}. \tag{1.2}$$

If time reversal symmetry is broken, for example if a ferrite is present, the probability distribution has the form

$$P_{GUE}(s) \cong \frac{32}{\pi} s^2 \exp(-4s^2/\pi). \tag{1.3}$$

The probability distributions apply to the eigenvalues of matrices that are from the Gaussian orthogonal ensemble (GOE) or Gaussian unitary ensemble (GUE). These have been shown to be applicable in enclosures that are "ray chaotic." That is, in the limit where the incident wave propagates like a point particle, the ray trajectories are chaotic [20].

In practical systems, however, the universal distribution described above need to be combined with system specific parameters, which forms the random coupling model. This is discussed in the next section.

1.3 System Specific and Universal Parameters

The random coupling model is a statistical model used to characterize the impedance matrix of a multi-port, complex, overmoded electromagnetic cavity [10–12]. It is based on a combination of the random plane wave approximation, in which the fields at any point in the enclosure consist of the random superposition of isotropically propagating plane waves with random phases, and the random matrix theory which provides the statistical distributions. The main result from the random coupling model [10] is that the random impedance, Z, at a port in a wave chaotic cavity is given in terms of system specific deterministic quantities and a universally distributed random quantity expressed in the following formula.

$$Z = jX_{rad} + \xi R_{rad}, \tag{1.4}$$

where R_{rad} and X_{rad} are the real and imaginary part of the radiation impedance (Z_{rad}), which is the impedance of the port excluding contributions from the cavity. In other words, it is the impedance that would be measured if the cavity walls were moved out to infinity. The quantity ξ is a complex random variable whose probability distribution is fully characterized by a single loss parameter (α). It is defined as

$$\xi = -\frac{j}{\pi} \sum_n \frac{\Delta k^2 \phi_n \phi_n^T}{k^2 - k_n^2 + j\alpha\Delta k^2}, \tag{1.5}$$

where ϕ_n is a vector of independent and identically distributed, zero mean, unit variance Gaussian random variables [21]. k_n^2 is also a random vector of the eigenmodes of the system whose normalized distribution is described by random matrix theory. A method to generate an ensemble of k_n^2 is described in Appendix A of Ref. [22]. The loss parameter, α, characterizes the loss in the enclosure and is described in detail in Chapter 2. This result can be extended to a multi-port cavity,

$$\mathbf{Z} = \mathbf{jX_{rad}} + \mathbf{R_{rad}^{1/2}} \xi \mathbf{R_{rad}^{1/2}}, \tag{1.6}$$

where all the variables are now matrices. Therefore, the quantities Z_{rad} and α are the two system specific parameters necessary to apply the random coupling model which allows us to predict the statistics of the impedance.

1.4 Outline of the Dissertation

Applying the random coupling model to real world enclosures presents challenges which I will discuss in the following chapters of the dissertation. The primary goal of my research is to formulate a methodology that allows an engineer to obtain the previously defined system specific parameters and to introduce additional parameters as necessary to characterize coupling statistics. In the following chapters of this dissertation, I will discuss methods I've studied over the course of the past six years to statistically characterize electromagnetic coupling in complex enclosures. In Chapter 2, I discuss the time gating technique as a measurement method to obtain the loss parameter and radiation impedance, but also as a tool to handle departures from the RCM due to short ray paths from a transmitting to receiving antenna.

In Chapter 3, I will discuss lossy antennas, a situation that was not previously addressed in the RCM. I will provide theoretical basis to allow another parameter, the radiation efficiency, to be added to the RCM. Experimental validation is also included. In Chapter 4, the limitation of the RCM are explored. The assumptions of the RCM of random plane wave hypothesis and overmoded cavity breakdown at low frequencies We discuss these limitations and the resulting lowest usable frequency for the RCM. In Chapter 5, I discuss a project in which we use the methods and tools established in the previous chapters to study the quantum mechanical phenomenon of regularization of quantum tunneling rates in chaotic cavities. The phenomenon is studied in an analogous system of microwave cavities. The theory and the validating experimental results are discussed in this chapter. Finally, in Chapter 6, I will provide a conclusion that ties together results of my research and discusses a direction for future projects.

Chapter 2: Extraction of the Coupling Impedance in Overmoded Cavities

2.1 Introduction

The coupling of electromagnetic field energy into and out of enclosures such as electronics cases, rooms and compartments, and reverberation chambers depends sensitively on the details of the enclosure's geometry and on the frequency of the injected radiation. Because of this sensitive dependence, a statistical description of the system's response is often sought [1]. The random coupling model (RCM) introduced for electromagnetic problems [10,11,13,23] and reviewed recently [21,22] has been successfully demonstrated to describe the statistics of a system's impedance matrix relating the currents and voltages at identified ports. The RCM is based on previous work in the theoretical physics literature [24–26]

There are certain assumptions that need to be met for RCM to apply. The first assumption is that the enclosure is electrically large. In other words, the wavelength of interest must be sufficiently small that the port excites many modes in the cavity. Only then can a statistical approach such as the RCM be considered. Second, the enclosure must have ray chaotic dynamics. This means that in the small wavelength

limit where the launched waves in the enclosure can be thought of as rays, the dynamics are chaotic. By "chaotic" we mean to say that if two rays are launched with a very small difference in the launch angle or location the trajectories diverge from one another exponentially. Typically, this requires the rays to strike a curved surface. These assumptions ensure that the field distributions in the enclosure have the local character of a random superposition of plane waves and that the resonant frequencies have a characteristic distribution described by random matrix theory [27]. The third assumption and the topic of this chapter is that the conditions of the ports are known and can be treated deterministically. The random nature of the system dynamics arise from the random scattering of rays in the enclosure itself, but not the ports. For all the ports, either their exact geometry and material properties are known such that the impedance of the ports under anechoic conditions can be computed numerically or, more practically, the impedance can be measured.

In the random coupling model, the impedance of the port under anechoic condition is called the radiation impedance (Z_{rad}). This is the impedance that would be measured at the port if there were no reflection from the enclosure's distant internal boundaries. The random coupling model allows one to statistically characterize electromagnetic energy coupled from one port to another; and in the simplest case from one port back to itself. According to the RCM, the values of the impedance that are measured at a port of a cavity can be modeled by the random variable

$$Z_{cav} = R_{rad}\xi + jX_{rad}, \tag{2.1}$$

where R_{rad} and X_{rad} are the real and imaginary part of the radiation impedance; and ξ is a complex random variable obtained from random matrix theory whose statistical properties are fully characterized by a single loss parameter. The loss parameter is essentially the average Q-width of resonant modes in the cavity normalized to the average spacing between modes. The dependence of ξ on this loss parameter is described in Ref. [10]. In the lossless case it is purely imaginary and Lorentzian distributed. As loss increases, the real part of ξ approaches unity with small Gaussian fluctuations, and the imaginary part of ξ approaches zero with small independent Gaussian fluctuations. Thus, in this limit the cavity impedance approaches the radiation impedance. Equation 2.1 applies to the case of a single port and determines a scalar impedance. For a cavity with multiple ports there is a simple matrix generalization of Eq. 2.1 in which the quantities are matrices and the first term is written $\boldsymbol{R_{rad}}^{1/2}\ \boldsymbol{\xi}\boldsymbol{R_{rad}}^{\ 1/2}$.

There have been two methods suggested to measure the radiation impedance. The first method is to line the enclosure walls with radiation absorbing material, and is the method used by Hemmady et. al [23]. in experiments to validate the RCM. This method can be time consuming and requires access to the interior of the enclosure. Furthermore, this method requires assigning a portion of wall of the enclosure in proximity to the port. This boundary where a port ends and the enclosure begins may be difficult to determine. The other method is to use a mode stirrer inside the enclosure and collect an ensemble of impedance measurements. The average of a large ensemble of measurements will converge to the radiation impedance. This requires that the mode stirrer sufficiently mixes the modes in the

enclosure and that a large enough ensemble is sampled; both of which are difficult to realize in practical enclosures. On the other hand, the time gating method described in the following sections only requires a single measurement at the port. Access to the interior of the enclosure is not required. The characteristic reflections from the nearby enclosure walls can be adjusted by a single parameter: the gating time. The implementation of the time gating method will be discussed in this chapter. The chapter is organized as follows. The time gating method and it's implementation to measure the RCM parameters are described in sections 2.2 and 2.3. Results from experimental validation of the method are presented in section 2.4. A discussion of the potential sources of error in time gating and solutions including a treatment of the localized power loss at the port are presented in section 2.5. Finally, the main ideas are summarized in section 2.6.

2.2 Time Gating Method

Time-gating is a method by which a frequency domain measurement is effectively averaged over a sliding window in the frequency domain. The method applies the Fourier transform of the measured complex reflection coefficient to the time domain, gating it in time, and Fourier transforming back to the frequency domain. If T_G is the duration of gating, then T_G^{-1} is the effective width of the frequency window. The purpose of the time gating presented here is the determination of the radiation impedance of the port including the effect of nearby reflections and excluding the effect of multiple far field reflections.

Time gating has been used for decades to improve frequency domain measurements [28]. In an antenna pattern measurement, the time-gating method (TGM) is used to remove unwanted multipath reflections from structures near the antenna [29, 30]. Ideally an antenna pattern is measured in an anechoic chamber where reflections from the walls are suppressed by radiation absorbing material. However, if an anechoic chamber is not available, or if the absorbers are not well suited for the frequency range of interest, there will be unwanted reflections from the walls. This is where the TGM can be used to suppress the reflections from the walls. In addition to this, it is also used to characterize reverberant chambers [31]. In this case, the information that characterizes the reverberant chamber is found in the difference between the ungated and the time gated measurement. In these cases, the TGM has been a valuable tool.

The TGM is implemented in some modern vector network analyzers (VNA). In a VNA, the reflection coefficient is measured in the frequency domain using a swept CW source and a receiver that tracks the amplitude and the phase of the received signal. The TGM method process is shown in Eq. 2.2.

$$\begin{aligned} \bar{S}(f) &\xrightarrow{\mathcal{F}^{-1}} s(t) \\ s(t)\, g(t) &\xrightarrow{\mathcal{F}} \bar{S}_g(f) \end{aligned} \tag{2.2}$$

The complex reflection coefficient $\bar{S}(f)$ is transformed to the time domain using an inverse fast Fourier transform (IFFT). This time domain signal $s(t)$ is multiplied by a gating window function $g(t)$ to select the duration of the time window of interest and suppress the rest. The gated time domain signal is Fourier transformed back to the frequency domain to arrive at the desired result $\bar{S}_g(f)$.

Another way to implement the TGM, is to use the fact that multiplication in the time domain is equivalent to a convolution in the frequency domain. The time domain gating window is transformed to the frequency domain using a fast Fourier transform (FFT) and convolved with the raw frequency domain measurement. The result is the gated reflection coefficient. This can be expressed as,

$$\bar{S}_g(f) = \bar{S}(f) \otimes \bar{G}(f) \tag{2.3}$$

where $\bar{S}(f)$ is the unprocessed frequency domain S-parameter measurement, $g(t)$ is the gating function in time and $\bar{G}(f)$ is its Fourier transform, and $\otimes$ is the convolution operator.

One of the advantages of the TGM is the flexibility in being able to choose a gating time and gating function to include the effect of prominent reflections. After collecting reflection coefficient data over the frequency range of interest, we Fourier transform the data into the time domain. A plot of the time domain data allows us to visualize the dominant reflections along the signal path. For example, results of a measurement of the reflection coefficient from an antenna radiating into a cavity are shown in Fig. 2.1. In this example, an L-band helical antenna irradiates a 3 m^3 aluminum cavity. We can see that there is a clear prompt reflection from the antenna centered at $t = 0$ [ns]. This prompt reflection gives us valuable information about the port; namely, how much power enters the cavity.

If we set the gating time to include only this peak, and transform back to the frequency domain, we obtain a reflection coefficient that is window-averaged over a broad frequency range. This window average eliminates important structure

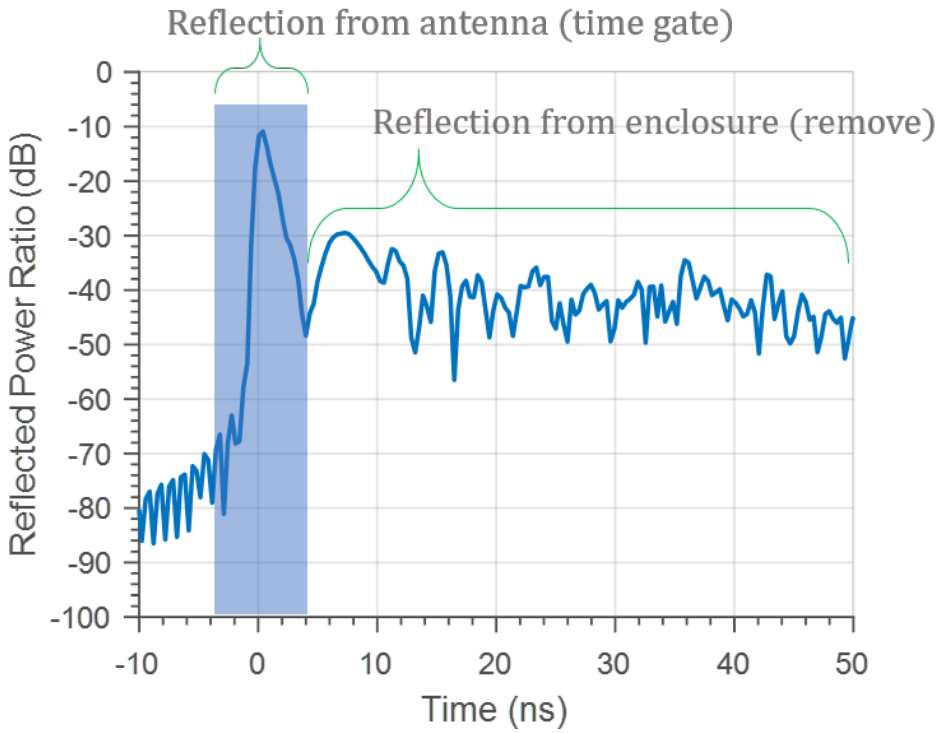

Figure 2.1: A power delay profile obtained by Fourier transforming the reflection coefficient of the antenna radiating inside a reverberant enclosure. The first peak comes from the antenna and subsequent peaks are reflections from the enclosure walls.

in the reflection coefficient associated with reflections from nearby walls [32, 33] . Returning to the time domain, Fig. 2.1 for some time after the prompt reflection, $t > 5ns$, there are many strong temporal peaks or reflections from the cavity that give rise to systematic variations of the reflection coefficient with frequency. When measuring the radiation impedance (associated with prompt reflection), these later reflections are removed: for this example, we might choose a gating time to be $5ns$, however, if we desire to average over a smaller frequency range, and thus include multiple reflections from the nearby walls, we can do so by further increasing the gating time. This is addressed in section 2.3. Once we have decided on the gating time, we need to select a gating function. If we use a rectangular windowing function in time, then in the frequency domain the measurement is convolved with a sinc-function, which has alternating positive and negative lobes. If we use a Gaussian window, then the windowing function is a Gaussian and is always positive. For simplicity, we will use a rectangular function in this chapter such that the gating is given by,

$$g(t) = \begin{cases} 1 & : t < T_G \\ 0 & : t \geq T_G \end{cases} \tag{2.4}$$

where T_G is the gating time.

2.3 Determination of Z_{rad} using TGM

We illustrate the time gating method by considering a particular antenna. We measure the impedance of an L-band helical antenna in a mode stirred rectangular

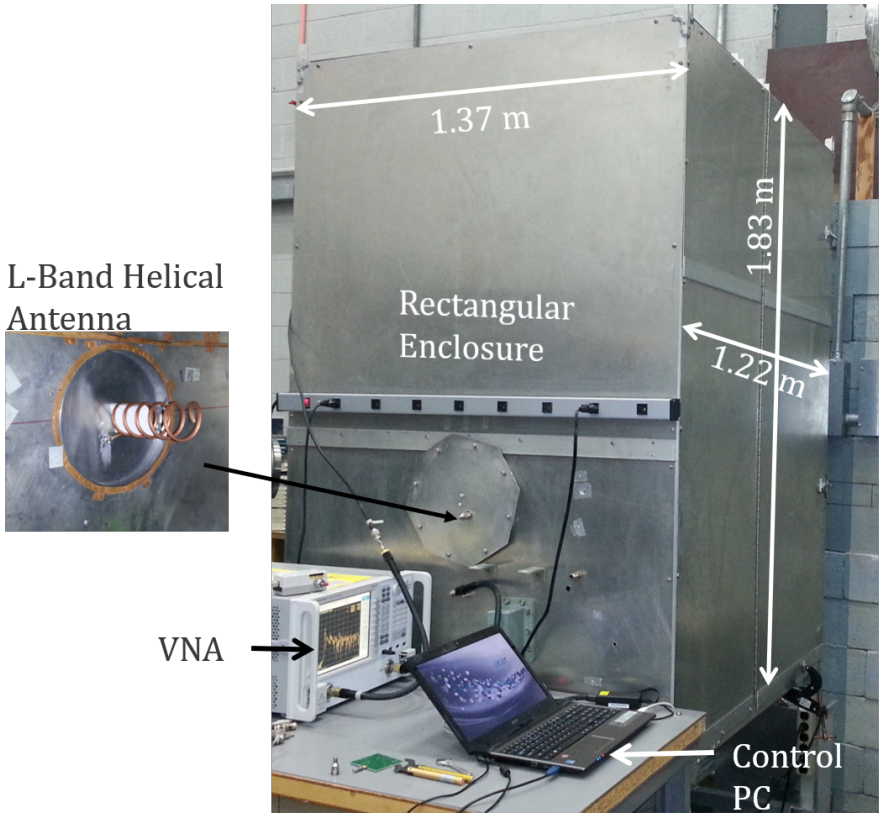

Figure 2.2: The measurement setup showing the rectangular enclosure, the VNA to make the measurements, and the control PC to collect and analyze the measurements.

reverberant chamber shown in Fig. 2.2. This aluminum enclosure has dimensions 1.37m x 1.22m x 1.83m for a volume of 3.06 cubic meters. The helical antenna is made from quarter inch copper tube, 24.1 cm in length. The measurement is taken over the frequency range of 1.5 GHz to 3.5 GHz, over which the RCM loss parameter (α) is measured to be 2.8. The loss parameter is given by

$$\alpha = \frac{\omega}{2\Delta\omega Q} \tag{2.5}$$

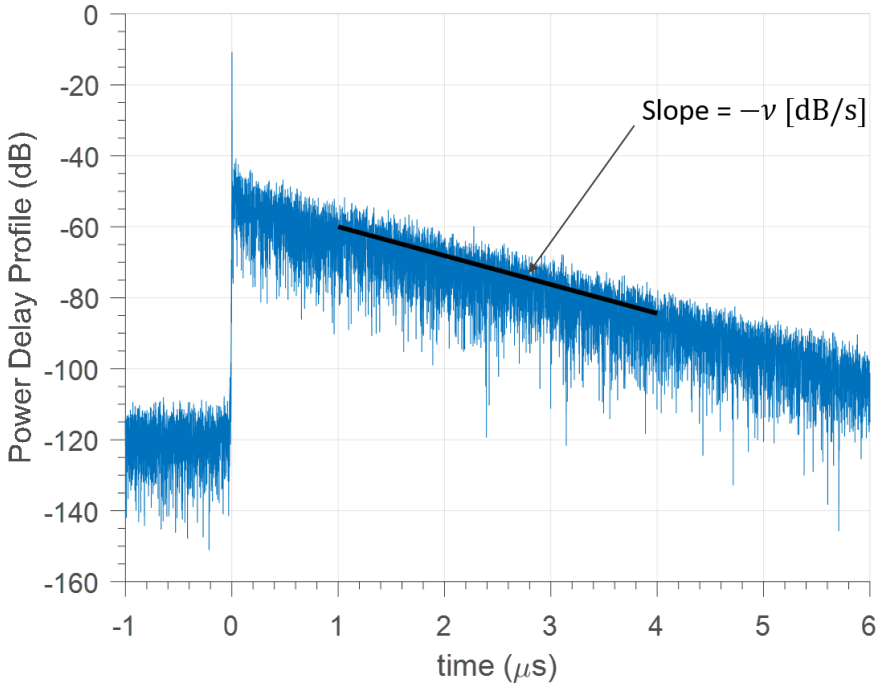

Figure 2.3: The power delay profile computed by Fourier transforming the reflection coefficient. The slope is used to compute the energy decay time constant (τ).

where ω, Q, $\Delta\omega$ are the angular frequency and the quality factor and the average mode spacing, respectively. The quality factor is measured from the energy decay time constant (τ) for the enclosure from which

$$Q = \omega\tau. \tag{2.6}$$

The energy decay time constant is obtained by Fourier transforming the measured reflection coefficient (S_{11}) to the time domain, then squaring the result. The squared result is referred to as the power delay profile. The power delay profile from a single measurement as function of time is shown in Fig. 2.3. The slope is computed during the 1 μs - 4 μs period by smoothing average of the power delay

profile. The slope (-ν [dB/s]) is then used to compute time constant quantity factor which in this case is measured to be 7980.

$$\tau = 4.34/\nu. \tag{2.7}$$

The mean mode spacing, on the other hand, is determined theoretically using Weyl's formula [19] given by

$$\Delta\omega = \frac{\pi^2 c^3}{\omega^2 V}, \tag{2.8}$$

where c and V are the speed of light and the volume of the cavity, respectively. The mode stirrer consists of a sheet of aluminum held at a 45 degree angle on shaft that is rotated by a programmable stepper motor. We generate 50 cavity realizations for 50 distinct positions of the mode stirrer. Figure 2.4 displays three version of the magnitude of the reflection coefficient, $|S_{11}|$. Shown in light gray is the reflection coefficient obtained from one position of the stirrer. Shown in red is the average reflection coefficient obtained by averaging $|S_{11}|$ over the 50 stirrer positions. The black solid curves and the black dashed line are the reflection coefficients obtained using the TGM as follows.

To obtain the window averaged reflection coefficient using TGM one must select a gating time. The effect of varying the gating time is to include or exclude contributions to the reflection coefficient from the ray paths or orbits that leave the antenna, bounce off a wall, and return. The effect of the orbits is specific to the cavity under consideration and not included in the model impedance, Eq. 2.1. The treatment of the orbits, called short orbits was addressed theoretically by Hart et al. [33] and impelemented by Yeh et. al [32]. The approach is to replace Z_{rad} in

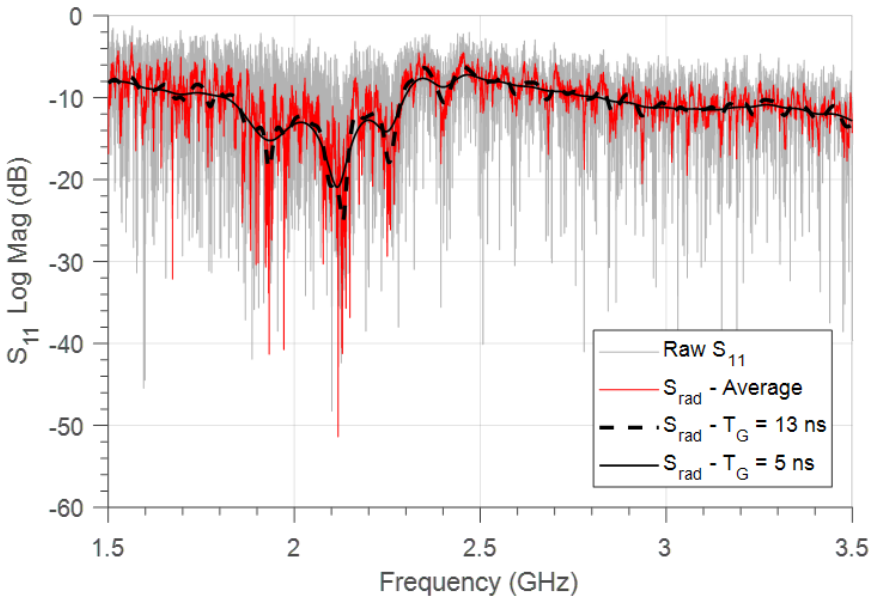

Figure 2.4: The radiation scattering parameter (S_{rad}) obtained as follows: gray a single realization, red- averaging over an ensemble of 50 cavity realization obtained by rotating the stirrer, black obtained from TGM (solid $T_G = 5$ ns , dashed $T_G = 13$ ns).

Eq. 2.1 by Z_{avg} where Z_{avg} is a frequency window average of the raw impedance matrix. In principle, there are mathematical formulas for Z_{avg} involving summations of contributions from a small number of ray paths [32,33]. To do this using TGM we look at the power delay profile in Fig. 2.1. We set the delay window time to $T_G = 13$ ns and inverse Fourier transform to obtain the TGM reflection coefficient shown as the dashed curve in Fig. 2.4. For comparison, the reflection coefficient using a windowing time of $T_G = 5$ ns is also shown in Fig. 2.4. The reflection coefficient has significantly less structure in frequency that either the ensemble average reflection coefficient or the TGM, $T_G = 13$ ns reflection coefficient. This will be of significance when we characterize fluctuations about the average impedance in the next section.

2.4 Impedance Fluctuations

We measure frequency scans of the reflection coefficient for 50 positions of the stirrer. In addition, we apply TGM to one of these scans using Eq. 2.3 with two different gating times, $T_G = 5$ ns and $T_G = 13$ ns. We convert these frequency dependent reflection coefficients to the frequency dependent impedances using,

$$\frac{Z_{cav}}{Z_0} = \frac{1 + S_{11}}{1 - S_{11}} \tag{2.9}$$

where $Z_0 = 50\Omega$ is the characteristic impedance of the transmission line feeding the antenna. We then normalize the measured values of the impedance using the formula implied by Eq. 2.1,

$$\xi_m = \frac{Z_{cav} - j\bar{X}}{\bar{R}}, \tag{2.10}$$

where Z_{cav} are the raw measurement of the input impedance at the port and $\bar{Z} = \bar{R} + j\bar{X}$ is either the radiation impedance Z_{rad} ($T_G = 5$ ns) or the TGM determined impedance Z_{avg} ($T_G = 13$ ns).

According to RCM the values of ξ_m should behave as random variables with a probability density function that depends on the loss parameter (α), which is measured by the method discussed in section 2.3 to be 6 for the frequency range of 3 GHz to 3.5 GHz. The quantity ξ_m is computed from the measured Z_{cav} and normalized by Z_{rad} ($T_G = 5$ ns). We compare the distribution of ξ_m with the RCM prediction. The predicted distribution is obtained from the Monte Carlo simulation described in Appendix A of [22]. The two distributions of the real and imaginary part of the normalized impedance (ξ) are good agreement as shown in Fig. 2.5.

Over the frequency range 2.245 GHz and 2.265, The loss parameter α is 2.3. In this 20 MHz window, as shown in Fig. 2.6, there is a significant difference between the radiation impedance and the TGM acquired impedance with $T_G = 13$ ns. This will affect the distribution of ξ_m as given by Eq. 2.10. Three pdfs of the real and imaginary part ξ_m using Eq. 2.10 are shown in Fig. 2.6. The pdf that is in best agreement with the predicted pdf is obtained from ξ_m that is normalized with the TGM determined impedance using a time window that includes short orbits ($T_G =$ 13 ns). The agreement with its prediction is better than the impedance normalized with the radiation impedance ($T_G = 5$ ns). These results confirm the RCM statistical model can be applied provided that the appropriate average impedance is used in Eq. 2.10 to normalize the measured values of cavity impedance.

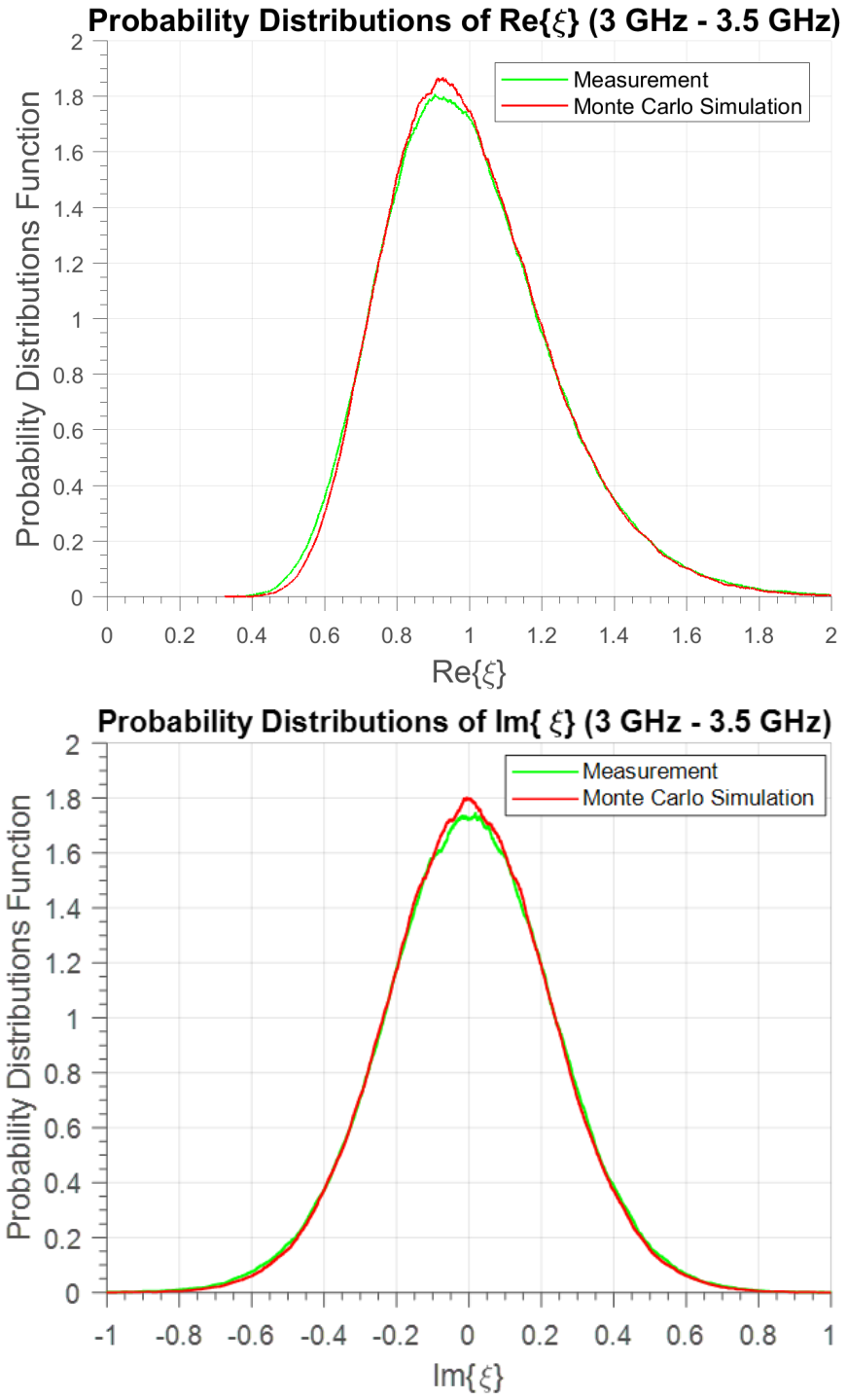

Figure 2.5: A comparison of the real (top) and imaginary (bottom) part of the measured and computed normalized impedances over the frequency range 3 GHz 3.5 GHz.

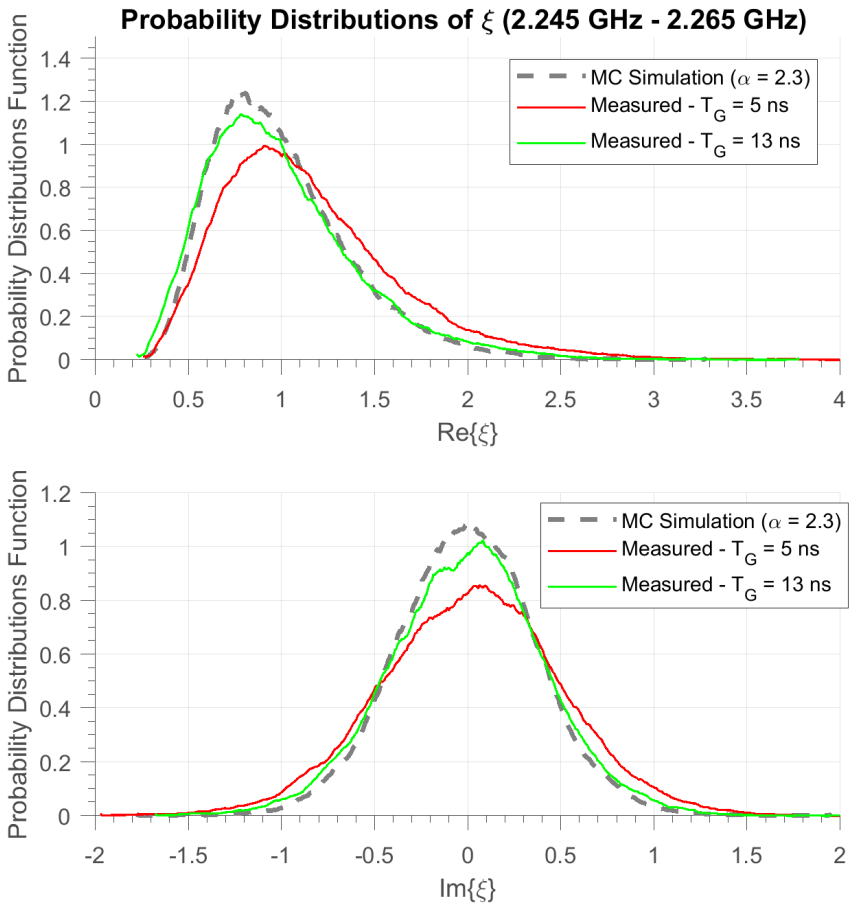

Figure 2.6: A comparison of the pdfs of the real (top) and imaginary (bottom) part of the measured and computed normalized impedances over the frequency range 2.245 GHz -2.265 GHz where the short orbits have a stronger effect of the pdfs.

2.5 Discussion

The results of the previous section show that the measured values of the cavity impedance can be modeled by the RCM provided the appropriate values of the average impedance $\bar{Z} = \bar{R} + j\bar{X}$ is used in Eq. 2.10. This value of average impedance can be extracted using the time gating method (TGM). The possible errors in the TGM are discussed in the context of the early implementation of the TGM inside a network analyzer by Lu. et al. [34]. They have grouped them in four categories. The first is the out of gate attenuation error. This occurs if the gating window function is not equal to zero outside the gating window. In which case, it doesn't completely suppress the unwanted reflections. A rectangular window will avoid this error. However, the sharp edges of the rectangular window in the time domain can cause a ringing effect in the frequency domain. Modern VNAs often use other windowing function to balance the ringing effects while also minimizing the out of gate attenuation error. The second type of error is truncation error. This arises when there is an overlap in time between the desired signal and the signal we want to suppress. By suppressing the unwanted segment in time, we are also losing the tail of the signal of interest. This is important to keep in mind when deciding on the gating time. The third and fourth types of error are masking error and multi-reflection aliasing error. Both of which arise when we want to suppress the prompt reflection and keep the subsequent reflections. Therefore, it doesn't apply in this context.

Finally, the measurements of the radiation impedance assume negligible power

loss at the port. This means the incident power at the antenna is either promptly reflected or radiated into the cavity. Conversely, if the power is lost locally at the port due to a lossy antenna, the radiation impedance cannot be directly measured with TGM or any of the methods previously discussed. This situation is addressed by the authors of Ref. [35] and this is the subject of Chapter 3 of this thesis. The result in the high loss limit ($\alpha \gg 1$) is a new formulation of the RCM that includes the radiation efficiency (η) of the antenna. Updating Eq. 2.10 for the normalized impedance we find

$$\xi_m = \frac{Z_{cav} - j\bar{X}}{\eta \bar{R}} + \frac{(\eta - 1)}{\eta} \tag{2.11}$$

For example, we can consider a lossy antenna in the aluminum cavity discussed in section 2.3. A copper trace on FR4 circuit board forms a loop antenna that has some localized power loss in the frequency range of 3 GHz - 3.5 GHz. The antenna is simulated in ANSYS HFSS [36]. The radiation efficiency over this frequency fluctuates between 0.69 and 0.81 for an average of 0.75. Using this value, we normalize the impedance by applying Eq. 2.11. In Fig. 2.7, very good agreement is shown between the data normalized according to Eq. 2.11 with the prediction distribution of ξ computed for the measured loss parameter ($\alpha = 6$). Conversely, if we had assumed that the port had negligible loss and applied Eq. 2.10, the variance of the normalized impedance would be smaller due to the unaccounted-for port loss.

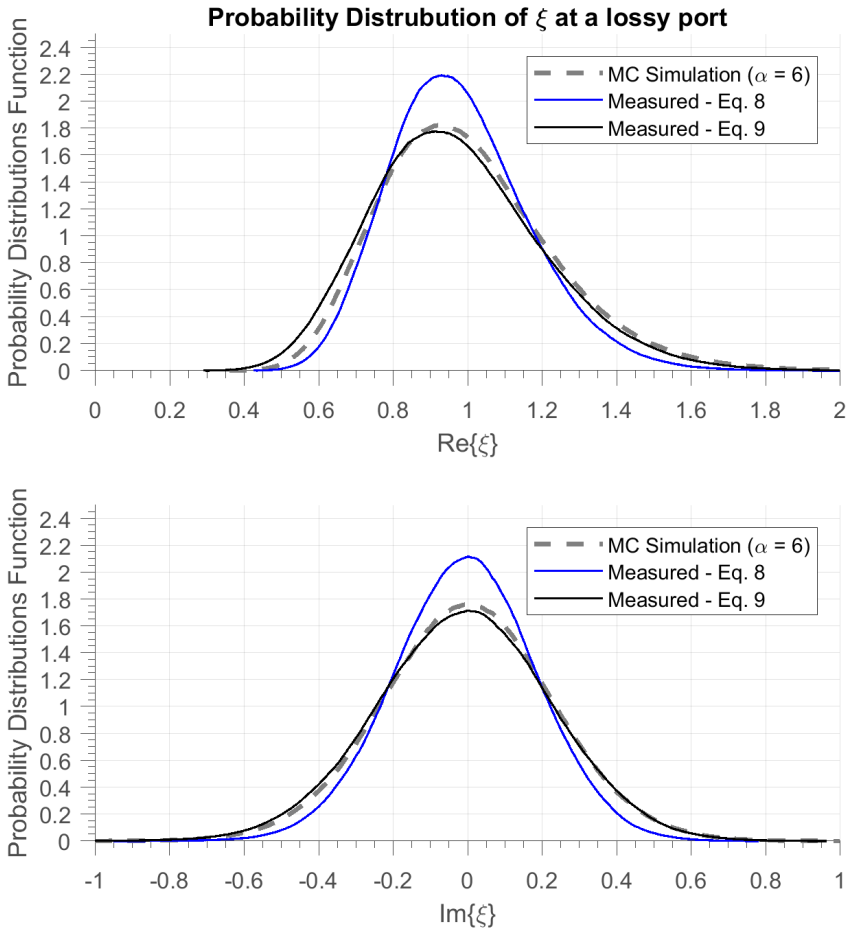

Figure 2.7: A comparison of the pdfs of the real (top) and imaginary (bottom) part of the measured and computed normalized impedances for a lossy port.

2.6 Conclusion

In this chapter, we presented a new way to measure the radiation impedance in the random coupling model using time gating method. It is shown to have the capability of including short orbits in the measurement. The method has been experimentally demonstrated and seems to be in good agreement with the predictions of the random coupling model.

Chapter 3: RCM for Ports with High Localized loss

In chapter 2, we discussed methods to extract the parameters of the ports and the enclosure. Once we have collected these deterministic parameters, we can form a complete statistical characterization of the EM wave system by using the random coupling model (RCM). However, in those descriptions and previous description of the RCM [10,21,22], the ports were such that the EM radiation incident at the port is either promptly reflected or radiated into the enclosure. The case in which EM radiation is dissipated locally at the port was not addressed. In this chapter, we will consider the case of lossy antennas. We will demonstrate not only the difficulty of measuring the radiation impedance parameter, but also the incorrect statistics that result if we use the traditional methods for measuring radiation impedance. Finally, a modified RCM model is derived with the introduction of the radiation efficiency to the model. Under the typical condition of a lossy cavity, the model can handle a port with high localized loss. Some of the contents of this chapter can also be found in [35].

3.1 Introduction

The RCM models the impedance statistics at the ports of a complex enclosure [22]. The formula for this impedance has been presented in Eq. 1.6. As it is, it is given in terms of two variables: the radiation impedance, Z_{rad}, and the random quantity, ξ, which depends on a single deterministic loss parameter, α. Therefore, for the RCM to be useful we require two deterministic parameters of the system, the radiation impedance and the loss parameter. However, a lack of direct measurement access to the enclosure and the ports, could make the RCM unusable. In chapter 2, the time gating method (TGM) is presented as a solution for measuring the radiation impedance of the ports in the case where direct access of the enclosure is not possible.

The radiation impedance is the impedance that would be measured at the ports if there were no reflection from the enclosure walls or if the walls were moved out to infinity. In previous tests of the RCM, the radiation impedance was measured by lining the walls of the enclosure with radiation absorbing material. The absorbers significantly dampened the reflections from the walls of the enclosure such that the impedance measured at the ports was the radiation impedance. However, lining the walls with absorbers is not always possible; thus the TGM as discussed in Chapter 2 is a method that does not require physical access to the interior of the enclosure walls used to determine the radiation impedance. Therefore, with access to only the terminals of the port, the radiation impedance could be measured. The situation changes, unfortunately, when ports with non-negligible localized loss are

considered. If there is significant localized loss at the port, the measured impedance at the terminal will not characterize the amount of power that enters the cavity. Rather, the antenna must be considered as a complicated network of impedances, a general model of which is detailed in 3.3.

These lossy ports, which may not be designed as antennas and to which we have limited access, are of great interest to the Electromagnetic Compatibility community [8]. Electromagnetic interference is often caused by strong electromagnetic energy coupling through unintended ports. The RCM's statistical description of such system is only applicable if we have access to measurements of the radiation impedance. In this chapter, we will describe a solution in the form of a modified RCM that accurately models the impedance of an enclosure with a lossy port.

This chapter is organized as follows. In Section 3.2, the different losses in the enclosure are described, including the losses through the ports. In Section 3.3, a detailed model of the lossy port is presented, as well as a modified RCM which uses measurements at the terminals of the port and the radiation efficiency of the port to form an accurate model of the impedance at a lossy port of a complex enclosure. In Section 3.4, the impedance measurement results of lossy ports are presented including comparisons to the predictive RCM model. Also, the methods of determining the radiation efficiency are described including numerical simulation and measurements. Finally, in Section 3.5 the main ideas and results of the chapter are summarized.

3.2 Loss in Reverberant Enclosures

In order to describe the losses in an electromagnetic enclosure, we use the dimension less quality factor parameter. The quality factor of an enclosure is defined as ratio of the electromagnetic energy stored in the enclosure to the power dissipated per cycle of the excitation frequency [37], written as,

$$Q = \frac{\omega U}{P_d}, \tag{3.1}$$

where U is the energy stored in the enclosure, P_d is the power dissipated, and ω is the angular frequency. In reverberant enclosures, electromagnetic energy dissipates through one of four loss mechanisms [38]. These loss mechanism are illustrated in Fig. 3.1. The power dissipated in the enclosure can written as,

$$P_d = P_{d1} + P_{d2} + P_{d3} + P_{d4} \tag{3.2}$$

where P_{d1} is the power lost through ohmic dissipation at the walls of the enclosure, P_{d2} is the power lost by loading objects in the enclosure such as microwave absorbers, P_{d3} is the power lost through apertures, and P_{d4} is the power lost through the ports. Therefore, by plugging Eq. 3.2 in Eq. 3.1, we can write the quality factor as

$$Q^{-1} = Q_1^{-1} + Q_2^{-1} + Q_3^{-1} + Q_4^{-1} \tag{3.3}$$

where,

$$Q_1 = \frac{\omega U}{P_{d1}}, Q_2 = \frac{\omega U}{P_{d2}}, Q_3 = \frac{\omega U}{P_{d3}}, Q_4 = \frac{\omega U}{P_{d4}}. \tag{3.4}$$

In the reverberant enclosures we study, the ohmic dissipation, P_{d1} and the power lost of objects in the enclosure, P_{d2} tend to be dominant. Furthermore, losses

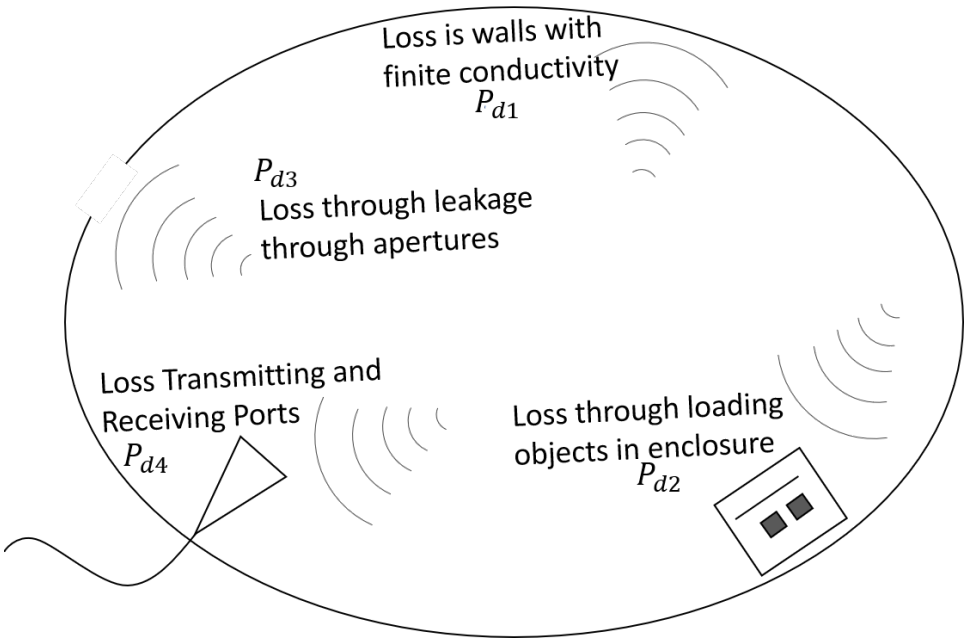

Figure 3.1: Multiple loss mechanisms in a reverberant electromagnetic enclosure.

through ports and apertures are treated separately in the RCM. For the stainless steel and aluminum enclosures in this thesis, and other highly conductive enclosures, Q_1 is given by the expression [39]

$$Q_1 = \frac{3V}{2\mu_r \delta A} \tag{3.5}$$

where V is the volume of the enclosure, A is the surface area of the walls of the enclosure, μ_r is the relative permeability of the metal, δ is the skin depth of the fields inside the metal walls. The other losses can vary depending of the size and effectiveness of the absorbers, the size of the various apertures, and the antenna efficiency of the ports, respectively.

The loss parameter, α, in the context of the random coupling model, is defined

in terms of the quality factor by the formula

$$\alpha = \frac{k^2}{\Delta k^2 Q} \tag{3.6}$$

where k^2 is the square of wavenumber, Δk^2 is the mean spacing between adjacent resonant modes, $k_{n+1}^2 - k_n^2$. The composite Q can be measured in the time domain from the exponential decay time constant as discussed in Chapter 2, in which α is approximated by Eq. 2.5. From the measurements in our enclosures, 2/3 of the total power dissipated in the enclosure is due to the ohmic loss at the walls. The power lost through the ports has minimal contribution due to the small effective aperture, regardless of the antenna efficiency or loss at the port. However, the loss at the port, as will be discussed in the next section, has a huge impact in our ability to measure the radiation impedance.

3.3 General Models of Lossy Port

Often ports in enclosures are antennas designed to have very low localized loss. For these types of antennas, the simple model shown in Fig. 3.2 applies, and we can measure the radiation impedance *in situ* by the time gating method described in Chapter 2. Therefore, in practice, a single port network analyzer measurement at the antenna over the frequencies of interest can capture the radiation impedance. Using the radiation impedance and the loss parameter, the impedance statistics at that antenna can be fully characterized.

However, there are other ports that are not designed for or intended to couple electromagnetic energy, which are also of interest to the EMC community [8]. Elec-

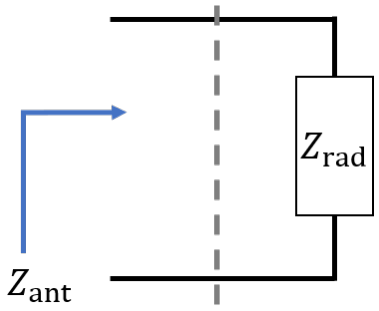

Figure 3.2: A simple model for an antenna with negligible loss. The time gated impedance measured at the port is the radiation impedance.

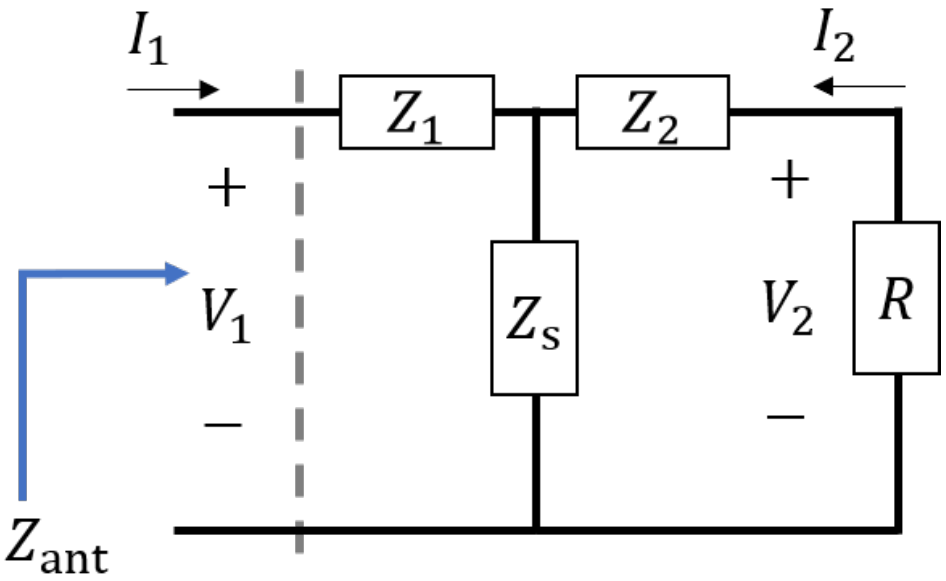

Figure 3.3: A generalized circuit model of the lossy port used for the impedance analysis. R is the radiation resistance and the radiation reactance is lumped with Z_2.

tromagnetic interference is often caused by strong electromagnetic energy coupling through unintended ports. In the most general case, antennas can be modeled by a "T-network" shown in Fig. 3.3, where Z_1, Z_2, and Z_s are complex impedances, and R is the radiation resistance and the radiation reactance is included in Z_2.

Thus, to characterize the antenna, three complex impedances values must be determined. These in principle are determined by exciting the two terminals of the network and measuring the currents I_1 and I_2. The loss can occur due to the resistance of any element in the branches of the T-network. If the antenna has significant localized loss the radiation impedance cannot be measured by the time gating method or by lining the cavity walls with absorbers. In this work, we consider the case when such a lossy antenna is located in an enclosure where the condition for the random coupling model applies. That is, the wavelength is large compared to the reverberant enclosure. In these enclosures, we often only have measurement access to Z_{ant}, (see Fig. 3.3) but we can't measure the additional impedances in the T-network. In this section, the impedance statistics are described for a single port enclosure such that the only additional information required is the radiation efficiency of the antenna.

The main result presented in this section is the following equation for the impedance of a lossy antenna attached to a complex enclosure.

$$Z_{in} = Z_{ant} + \eta Re\{Z_{ant}\}\delta\xi \tag{3.7}$$

where η is the radiation efficiency of the antenna. The quantity $\delta\xi$ is equal to $\xi - 1$ where ξ is the fluctuating normalized impedance as defined by Eq. 1.4. The quantity

Z_{ant} is the input impedance of the lossy antenna radiating in free space and will be defined in the derivation that follows.

For the following analysis, a two port model of the antenna shown in Fig. 3.3 is adopted. The elements of the two port impedance matrix are

$$Z_{11} = Z_1 + Z_s \tag{3.8}$$

$$Z_{22} = Z_2 + Z_s \tag{3.9}$$

$$Z_{12} = Z_{21} = Z_s. \tag{3.10}$$

When the antenna is placed in free space with no reflection, the measured input impedance is given as

$$Z_{in} = Z_{11} - \frac{Z_s^2}{Z_{22} + R} \equiv Z_{ant}. \tag{3.11}$$

The radiation efficiency of this antenna is defined as the ratio of the power radiated to the input power

$$\eta = \frac{P_R}{P_{in}}, \tag{3.12}$$

where $P_R = R|I_2|^2$ and $P_{in} = Re\{Z_{in}\}|I_1|^2$. Solving the circuit equations, we obtain the following expression for the radiation efficiency,

$$\eta = \frac{R}{Re\{Z_{ant}\}} \left| \frac{Z_s}{R + Z_{22}} \right|^2 \tag{3.13}$$

If this antenna is placed in a complex enclosure, we replace R with $R(1 + \delta\xi)$ in Eq. 3.11. For a typical high loss cavity where $\alpha \gg 1$ and $|\delta\xi| \ll 1$, the input impedance can approximated as follows,

$$Z_{in} \approx \left(Z_{11} - \frac{Z_{12}^2}{Z_{22} + R} \right) + \left(\frac{R Z_{12}^2}{(Z_{22} + R)^2} \right) \delta\xi. \tag{3.14}$$

Factoring out the phase from the second term, we obtain

$$Z_{in} = \left(Z_{11} - \frac{Z_{12}^2}{Z_{22} + R} \right) + \left| \frac{R Z_{12}^2}{(Z_{22} + R)^2} \right| \delta\xi\prime, \tag{3.15}$$

where $\delta\xi\prime = \delta\xi e^{j\phi}$ and ϕ is the phase of $RZ_{12}^2/(Z_{22} + R)^2$. Since $\delta\xi$ is approximated by a complex Gaussian random variable with independent and identically distributed real and imaginary parts, the phase of $\delta\xi$ will be uniformly distributed. This means that $\delta\xi$ and $\delta\xi\prime$ have the same statistical properties. Therefore we can drop the prime from $\delta\xi$ in Eq. 3.15. Now comparing Eq. 3.15 with Eq. 3.13, we arrive at the expression for the impedance given in Eq. 3.7 with quantities that can be easily measured.

3.4 Experimental Results for the Impedance Models at Lossy Ports

To demonstrate the effect of localized port losses, we focus on a copper loop antenna printed on a lossy FR4 based circuit board in Fig. 3.4. We measured this antenna inside a stainless steel cylindrical enclosure in Fig. 3.5 for two sets of frequencies. The loss parameters, measured according to Eq. 3.6, are equal to 1.6 and 24.1 for the frequency ranges 1.5 GHz to 3 GHz and 9 GHz to 11 GHz, respectively. The FR4 material has low dielectric loss in the lower frequency range, but the loss becomes significant at these higher frequencies, which reduces the radiation efficiency.

In order to measure the radiation efficiency, we first modeled the antenna and supporting material in ANSOFT High Frequency Structural Simulator (HFSS) [36]. Figure 3.6 shows the HFSS model for the antenna. An outgoing radiation boundary

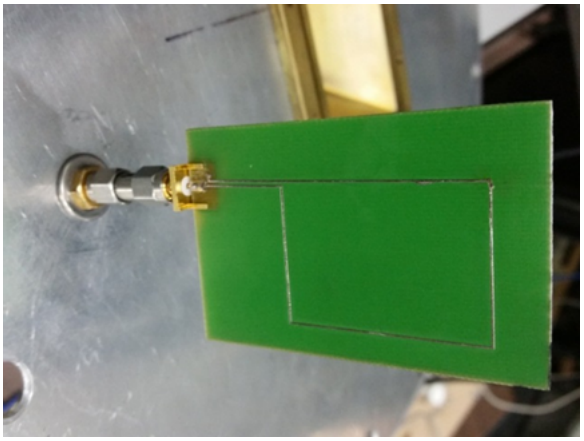

Figure 3.4: The copper loop trace on FR4 PCB used in the experiments.

Figure 3.5: The cylindrical stainless steel enclosure with a rotating mode stirrer.

condition is assigned to the large box surrounding the antenna. The radiation efficiency is computed as the ratio of the power radiated through the radiation boundary to the power incident at the input port of the antenna. Figure 3.7 and Fig. 3.8 show the resulting radiation efficiency computed for two frequency ranges. The average radiation efficiency is computed to be 0.56 and 0.81 for the frequency

ranges 1.5 GHz to 3 GHz and 9 GHz to 11 GHz, respectively.

In some cases, we do not have enough information about the antenna to simulate it in HFSS and compute its radiation efficiency. Under those circumstances, we use the statistics of the normalized impedance to measure the radiation efficiency. In Section 2.3, we discussed a method to measure the loss parameter, α, using the time constant for the exponential energy decay in the enclosure. Since the energy decay in the enclosure is dominated by loss mechanism other than loss at the port, this method can be used to measure α independent of the loss at the port. The variance of the normalized impedance of a lossless antenna in a lossy cavity has been shown in [12] to be a function of α. The variance of both the real and imaginary part of the normalized impedance is given by

$$\text{Var}\left[\xi_{\text{lossless}}\right] = \frac{1}{\pi\alpha}, \tag{3.16}$$

and it follows that by Eq. 3.7, the variance of the the normalzied impedance for a lossy antenna is

$$\text{Var}\left[\xi_{\text{lossy}}\right] = \frac{\eta^2}{\pi\alpha}, \tag{3.17}$$

Therefore, to measure η, we assume the antenna is lossless and normalize the measured impedance using Eq. 2.10. The quantity η is given by

$$\eta = \sqrt{\text{Var}[Re\{\xi_m\}]\pi\alpha}. \tag{3.18}$$

where ξ_m is the measured impedance normalized by Eq. 2.10 which assumes a lossless antenna. Using these radiation efficiency values, we can characterize the impedance statistics using Eq. 3.7.

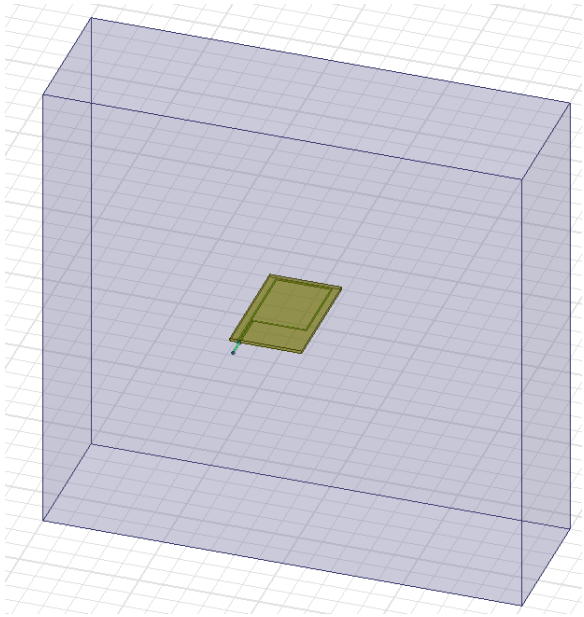

Figure 3.6: A copper loop trace on FR4 PCB modeled in HFSS inside a radiation box.

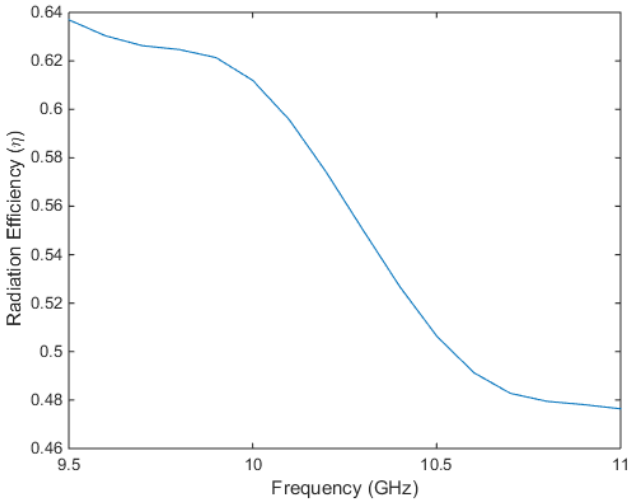

Figure 3.7: The radiation efficiency of the loop trace on antenna computed in HFSS for 9.5 GHz - 11 GHz.

The input impedance of this antenna is measured assuming the general antenna model in Fig. 3.3. This is done by directly measuring the reflection coefficient (S_{11}) using a vector network analyzer for 32001 points over the frequency range.

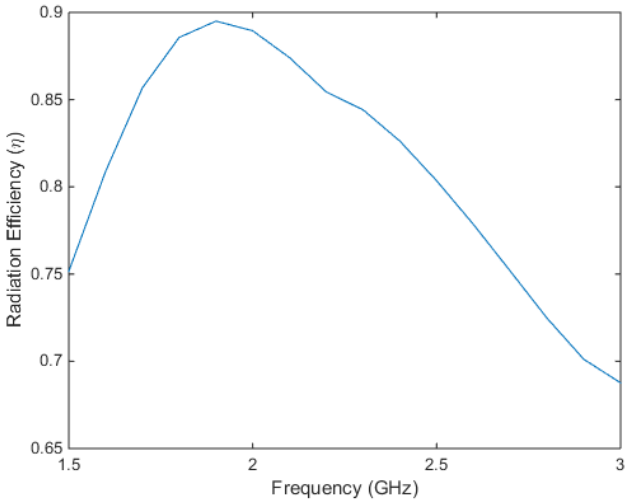

Figure 3.8: The radiation efficiency of the loop trace antenna computed in HFSS for 1.5 GHz - 3 GHz.

This measurement is repeated for 50 different positions of a mode stirrer inside the enclosure. Each position is 7.2 degree from an adjacent position which is roughly the minimum angular step required for uncorrelated measurements as discussed in Appendix A. The normalized impedance is computed for each measurement data point using Eq. 3.19, where the HFSS computed radiation efficiency is applied.

$$\delta\xi_M = \frac{Z_{in} - Z_{ant}}{\eta Re\{Z_{ant}\}} \tag{3.19}$$

Z_{in} is generated from the measured reflection coefficients, Eq. 3.20.

$$Z_{in} = Z_0^{\frac{1}{2}}(I - S_{11})^{-1}(I + S_{11})Z_0^{\frac{1}{2}} \tag{3.20}$$

Z_{ant} is computed from Z_{in} using the time gating method described is Chapter 2.

The probability density function (pdf) of the real and imaginary parts of the normalized impedance is generated from a histogram of the large ensemble of measurements. Figures 3.9, 3.10, 3.11, 3.12 show the pdfs are in good agreement with the predicted pdfs. The predicted pdfs are obtained from the random matrix based

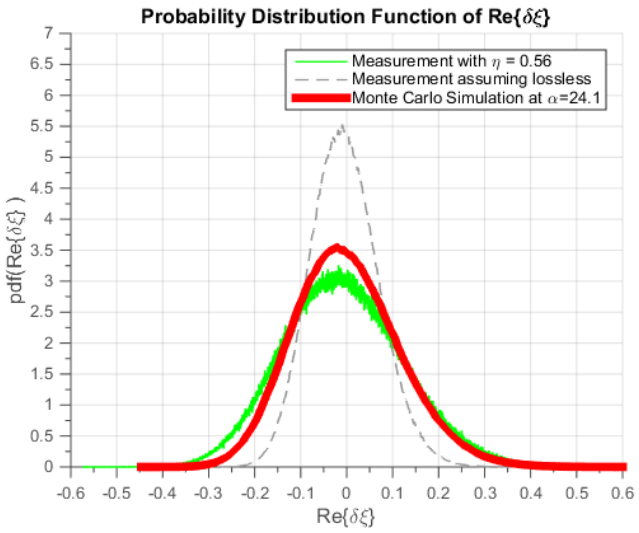

Figure 3.9: Comparison of the probability density function of the real part of the normalized impedance for 9.5 GHz - 11 GHz.

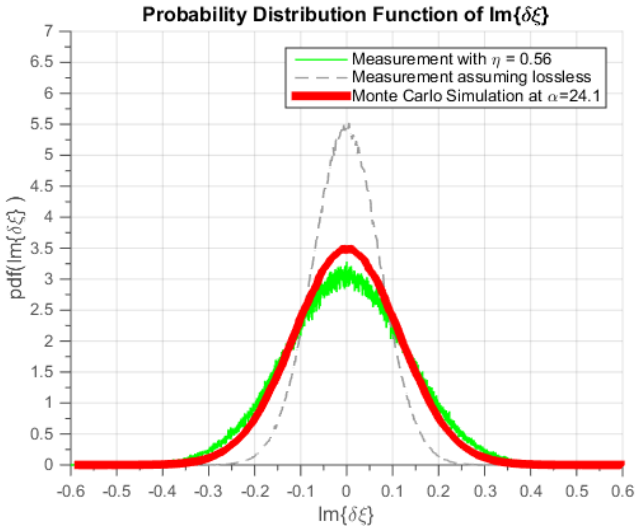

Figure 3.10: Comparison of the probability density function of the imaginary part of the normalized impedance for 9.5 GHz - 11 GHz.

Monte Carlo simulation [22], where the only parameter required for the Monte Carlo simulations is the measured loss parameter α. This agreement also shows the significance of this new model. That is, if we had assumed the simple low loss antenna model in Fig. 3.2, and would have obtained the pdfs, shown in gray in the Figs. 3.9, 3.10, 3.11, 3.12. These are shown to deviate substantially from the measured pdfs.

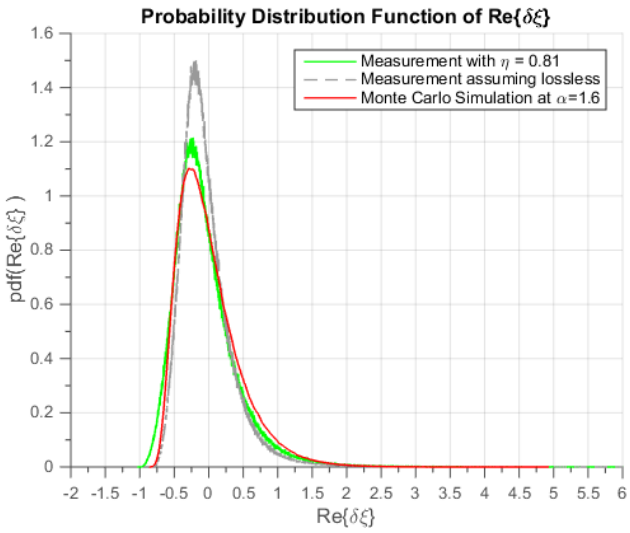

Figure 3.11: Comparison of the probability density function of the real part of the normalized impedance for 1.5 GHz - 3 GHz.

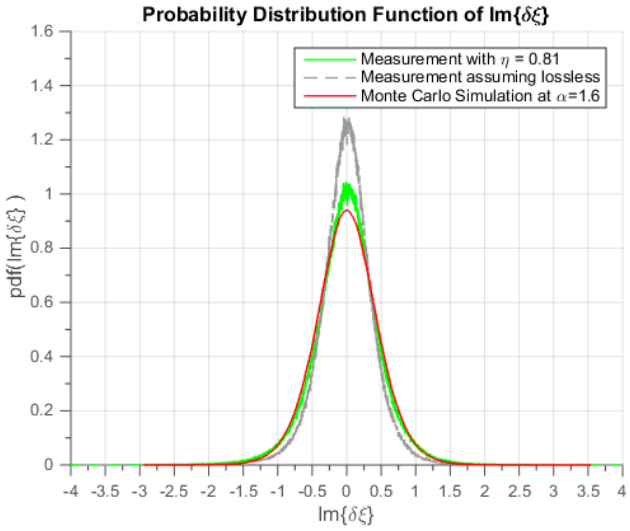

Figure 3.12: Comparison of the probability density function of the imaginary part of the normalized impedance for 1.5 GHz - 3 GHz.

3.5 Conclusion

We have shown that for a lossy antenna in a lossy cavity, the impedance statistics can still be characterized. Based on the description from the random coupling model and the use of the radiation efficiency, the probability density function of

the input impedance a port can be fully characterized. Furthermore, practical measurement techniques, that are of interest to EMC community are demonstrated for typical real world enclosures.

Chapter 4: Determining the Lowest Usable Frequency in the RCM

When using a statistical model such as the RCM it is important to know under what conditions the model is applicable to the system under consideration. The RCM is applicable to enclosures that display chaotic behavior in the small wavelength limit. For very small wavelengths, making a ray chaotic enclosure doesn't take much effort. For example, Haake et. al have demonstrated that even a cuboidal microwave chamber [40] with a monopole antenna whose diameter is on the order of a wavelength can produce spectra with the characteristic of a Gaussian orthogonal ensemble. On the other hand, for large wavelengths, even ray chaotic enclosures may not be described by wave chaos or the random coupling mode. This is because the assumption of ray trajectories ergodically filling the enclosure is invalidated at low frequencies. In this chapter, we discuss these assumptions of the RCM and present experimental metrics that can be used to determine the lowest usable frequency of the RCM.

4.1 Introduction

The random coupling model as described in Sec. 1.3 is a statistical model that describes the impedance at the ports of enclosures with a limited amount of

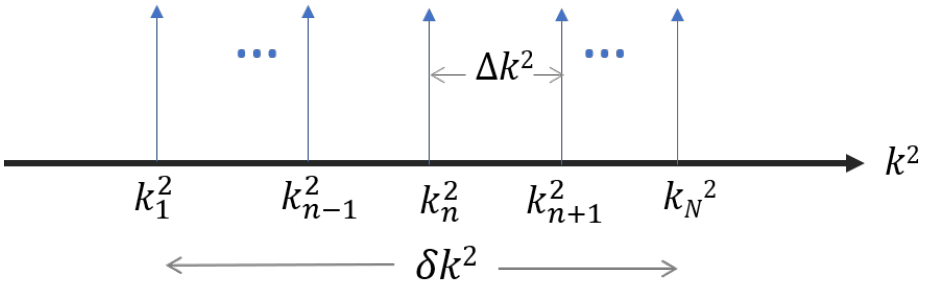

Figure 4.1: A illustration of the characteristic of an overmoded enclosure. For range of interest, δk^2, the enclosure is overmoded given $\Delta k^2 \ll \delta k^2 \ll k_n^2$

information about the enclosure itself. However, in order to apply the RCM, we must first verify two key assumptions about wave scattering within the enclosure [12, 20]. The first assumption is that the enclosure is overmoded. If we consider the complex random quantity ξ in the impedance formulation of the RCM,

$$\xi = -\frac{j}{\pi} \sum_n \frac{\Delta k^2 \phi_n \phi_n^T}{k^2 - k_n^2 + j\alpha/\Delta k^2}, \tag{4.1}$$

the comprising quantities of which are described in Sec. 1.3, the assumption is that there are many modes with k_n^2 over the frequency range of interest.

This is illustrated in Fig. 4.1, where $k = \frac{2\pi f}{c}$ is the wavenumber, f is the excitation frequency, and c is the speed of light. In the range δk^2 of k^2, over which we want to describe our system using the RCM, the assumption is that $\Delta k^2 \ll \delta k^2 \ll k_n^2$ such that within the range of δk^2 of k^2 many modes contribute to the response ($\Delta k^2 \ll \delta k^2$), but these modes have similar properties ($\delta k^2 \ll k_n^2$).

The second assumption is the "random plane wave hypothesis," which states the fields can be approximated as plane waves uniformly distributed in the enclosure

and locally can be treated as a superposition of isotropically propagating plane waves. This hypothesis is based on the ergodic nature of ray trajectories in chaotic billiards and has been demonstrated numerically for short wavelength solutions of the Helmholtz equation in [41]. This is also discussed in the context of tunneling in quantum wells [42]. The claim is that eigenfunction $\phi(\mathbf{x})$) of the Helmholtz equation can be approximated by a superposition of the plane waves with wavenumber k_n,

$$\phi(\mathbf{x}) = \sum_{j=1}^{N} a_j \cos\left(ik_n \hat{\mathbf{e}}_j \cdot \mathbf{x} + i\theta_j\right), \tag{4.2}$$

where the amplitude a_j is independent and identically distributed random variable, $\mathbf{e}_j$ is independent isotropically distributed random vector, and θ_j is independent and uniformly distributed random variable in $[0, 2\pi)$. Therefore, by the central limit theorem, for very large N, at any point $\mathbf{x}$, $\phi(\mathbf{x})$ will have a Gaussian distribution,

$$P_{\mathbf{x}}(\phi) = \frac{1}{\sqrt{2\pi\sigma^2}} \exp\left(\frac{-\phi^2}{2\sigma^2}\right). \tag{4.3}$$

However, this has only been validated at wavelengths much smaller than the enclosure dimensions. This approximations will be incorrect at wavelengths on the order of the size of the enclosure. Thus, it important to determine the lowest usable frequency.

The Electromagnetic compatibility (EMC) community also has this important task of finding the lowest usable frequency (LUF) in enclosures, where they test for immunity of electronic devices exposed to high power electromagnetic sources [44]. In order to test for a variety of attack angles over a wide range of frequencies, the devices are tested in mode stirred reverberation chambers similar to one shown in Fig. 4.2. As the mode stirrer rotates, and at high excitation frequencies, the fields

Figure 4.2: A example of a reverberation chamber at the Otto-von-Guericke-University Magdeburg, Germany, where electronic devices are test for immunity to high power electromagnetic sources [43]

at any point in the volume where the device is placed will have roughly uniform amplitude and isotropic direction, ideal for immunity testing. However, the uniformity and isotropy break down at lower frequencies. International standards [45] are written to guide users to determine the LUF for their enclosures. Some of the methods in the EMC community will be used in this chapter as we develop metrics to find the LUF of the RCM.

The chapter is organized as follows. In Section 4.2, an example case, a 2D chaotic cavity, is solved in ANSOFT HFSS to demonstrate the metrics that allow us to find the range of frequencies for which the RCM is applicable. In Section 4.3, we describe experimental methods to determine the LUF. The ideas in this chapter are summarized in Section 4.4.

4.2 Computing the distribution of field at lower frequency

In order to study the assumptions of the RCM at low frequencies, we simulate a classically chaotic bowtie shaped 2D cavity in ANSOFT HFSS [36]. The geometry of the cavity is shown in Fig. 4.3. The walls of the cavity are perfect electric conductors. We have added an elliptical mode stirrer that we rotate by 180 degrees in increments of 5 degrees. For each position of the mode stirrer, we solve for the first 40 eigenfrequencies. The size of the mode stirrer is made large enough to shift an eigenfrequency as it rotates by an amount equal to the spacing between eigenfrequencies. In the following, we describe the procedure used to determine the size of the mode stirrer.

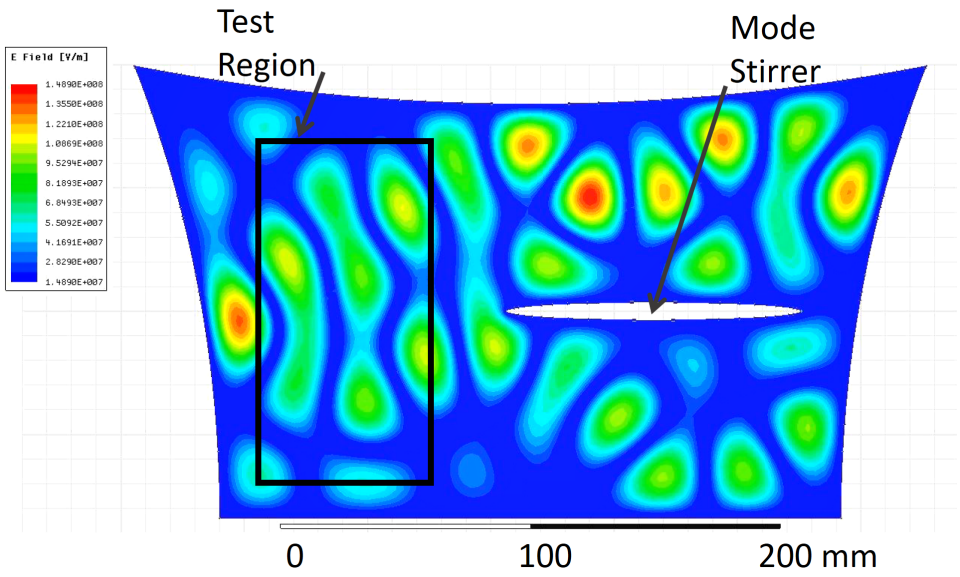

Figure 4.3: An example cavity simulated in HFSS. The fields are measured over the test region to verify a Gaussian distribution over an ensemble of mode stirrer positions

4.2.1 Determining the Size of the Mode Stirrer

We define the characteristic length of the mode stirrer to be

$$L_{\text{stir}} = \sqrt{A_{\text{stir}}}. \tag{4.4}$$

where A_{stir} is the circular area that the mode stirrer sweeps as it rotates. Similarly, the characteristic length of the bowtie cavity is

$$L_{\text{cav}} = \sqrt{A_{\text{cav}}}, \tag{4.5}$$

where A_{cav} is the area of the cavity. The area of the mode stirring ellipse is subtracted in calculating the area of the cavity. For the bowtie cavity shown in Fig. 4.3,

$L_{\text{cav}} = 21.5$ cm. The parameter of interest is the ratio of the characteristic lengths

$$R = \frac{L_{\text{stir}}}{L_{\text{cav}}}, \tag{4.6}$$

which could be used to determine the necessary size of mode stirrers in different shaped cavities as well.

For a range of values of R, we compute the first 20 eigenfrequencies of the bowtie cavity at each position of the rotating mode stirrer. For any one position of the mode stirrer, the mean spacing between squared eigenfrequencies is independent of frequency and given by the Weyl formula as

$$\left\langle \Delta F^2 \right\rangle_{\text{Weyl}} = \frac{c^2}{\pi^2 A_{\text{cav}}} \tag{4.7}$$

where c is the speed of light. As an example, the first 20 squared eigenfrequencies for $R = 0.5$ is shown in Fig. 4.4 as a function of the stirrer position. As we rotate the mode stirrer, the i^{th} squared eigenfrequency will vary over a range of squared frequencies, ΔF_i^2. We consider the cavity to be adequately stirred if R is large enough such that ΔF_i^2 averaged over i is greater than $\langle \Delta F^2 \rangle_{\text{Weyl}}$. For the cavity shown, $R = 0.5$ is large enough to satisfy this condition.

4.2.2 Electric Field Distribution in a Mode Stirred Cavity

Once we have set the geometry and the boundary conditions, we solve for the eigenmodes and evaluate the fields in the test region. This region is chosen not to be too close to any of the boundaries to avoid small field values. We compute the electric field in the test region shown in Fig. 4.4 on a rectangular grid with a spatial

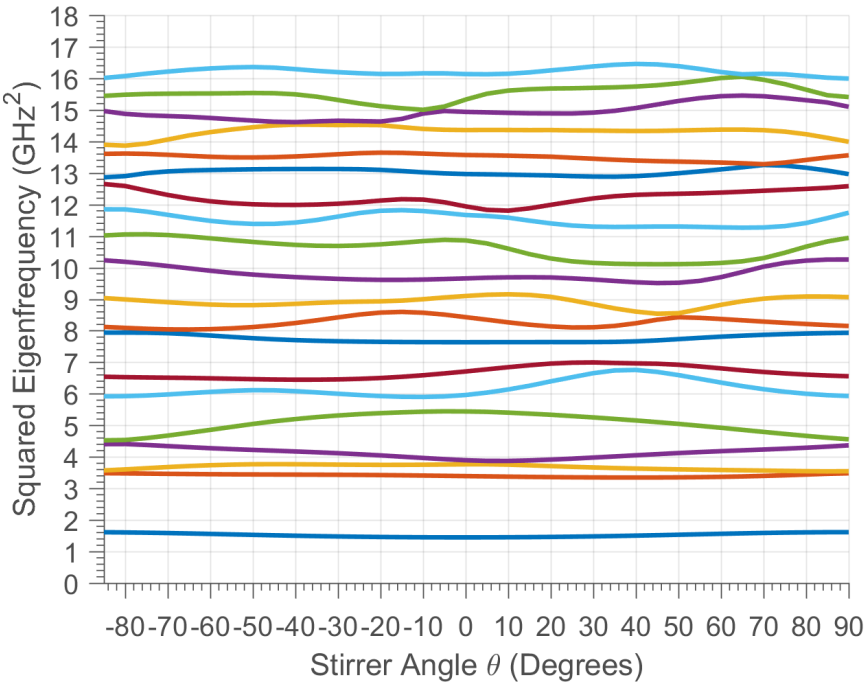

Figure 4.4: The first 20 squared eigenfrequencies in the bowtie cavity as a function of the angular position of the mode stirrer. The characteristic lengths ratio, $R = 0.5$

resolution of 1 mm at the first eigenfrequency above a specified frequency. By the random plane wave hypothesis, we expect the distribution of electric field to be Gaussian. Figure 4.5 shows the pdf of the electric field for two specified frequencies compared to a Gaussian distribution. At lower frequencies, such as 3 GHz where the ratio of the wavelength (λ) to the characteristic length of the cavity ($Ł_{\text{cav}}$) is 0.47, the pdf appears to deviate from a Gaussian distribution. At 6 GHz where λ/L_{cav} is 0.28, the pdf has a much better fit to a Gaussian. In order to determine the frequency below which the distribution of normalized electric field no longer fits a Gaussian, we apply the Kolmogorov-Smirnov goodness of fit test. The KS test statistic (D), is

$$D = \sup_x |F_E(x) - F_N(x)|, \tag{4.8}$$

where F_E is the cdf of the computed normalized electric field, F_N is the cdf of a standard Gaussian distribution, and sup is the supremum operator. The KS test statistic is shown in Fig. 4.6. Some the outliers at higher frequencies are cases where for some positions of the mode stirrer the eigenmodes are trapped on the right side of the mode stirrer and which never reach the test region and which have skewed the distribution of the electric field. For a 1% threshold, the lowest usable frequency is around 4 GHz where λ/L_{cav} is 0.35. Therefore, despite the fact that the cavity at these frequencies is not overmoded, the mode stirrer moves the eigenfrequencies enough that we have many different eigenfrequencies contained in the ensemble. The ensemble of electric fields at these eigenmodes have a Gaussian distribution which validates the random plane wave hypothesis.

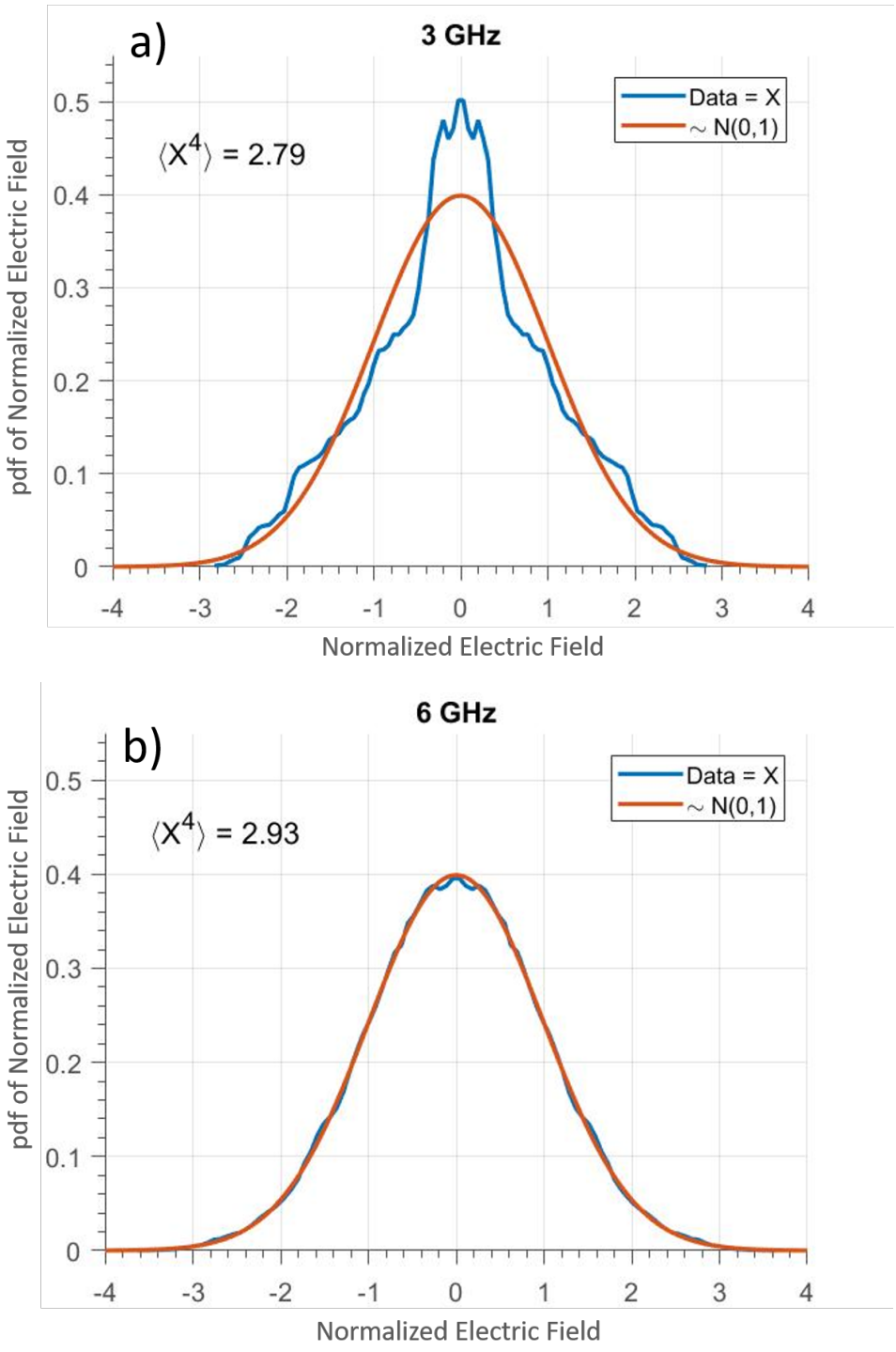

Figure 4.5: The probability density function of the real part of the normalized electric field over the test region. The electric field for the eigenmode closest to 6 GHz (b) appears to have a pdf closer to a Gaussian than the eigenmode closest to 3 GHz (a).

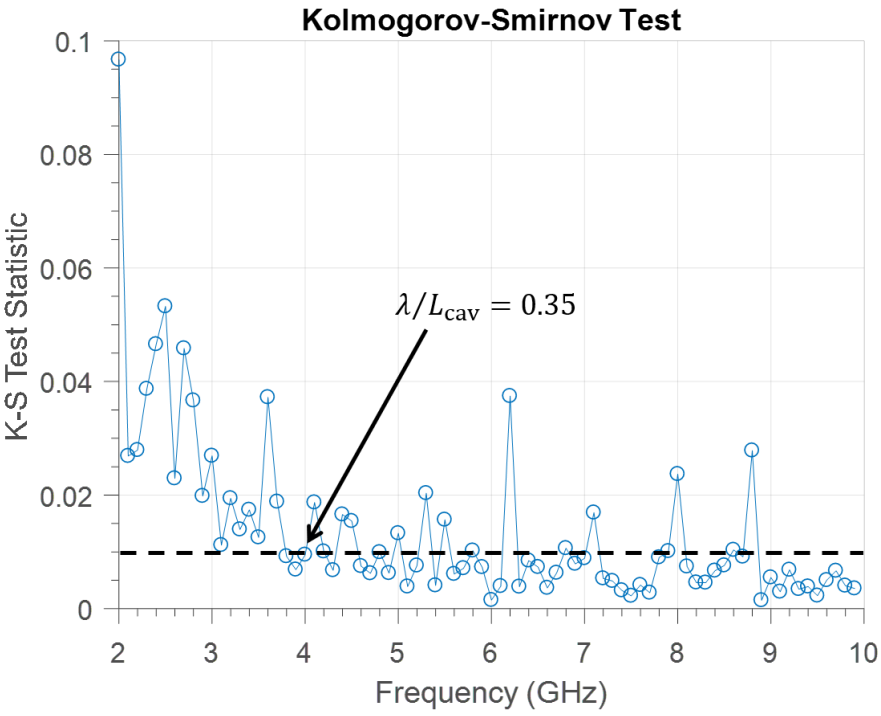

Figure 4.6: The Kolmogorov-Smirnov test of the electric field distribution in the cavity to the Gaussian distribution. The dash line is 1% threshold

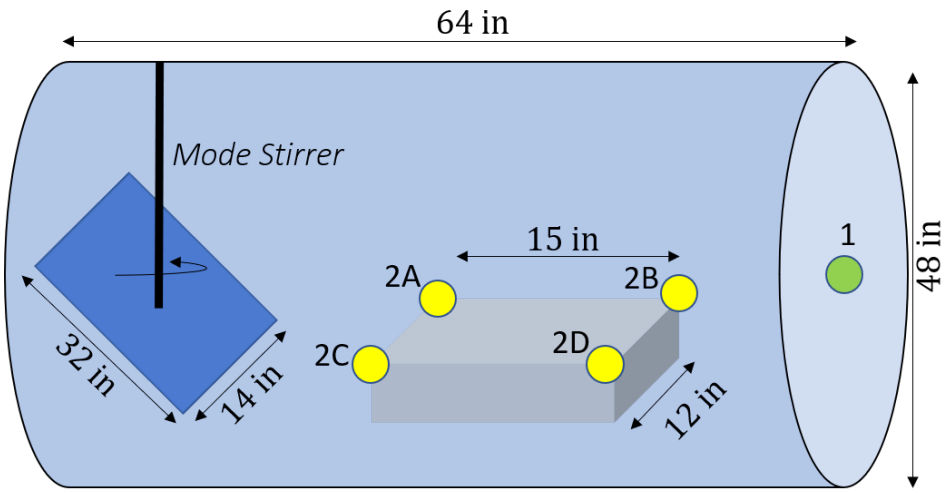

Figure 4.7: The cylindrical enclosure used for 2-port impedance measurements. Port 1 is stationary while the location of port 2 can be at one of four locations (2A, 2B, 2C, 2D).

4.3 Determining the lowest usable frequency in 3D Enclosures

For situations where we can not easily obtain the fields on a fine grid of points inside our enclosure, we need to look for some other metric. In the same cylindrical enclosure that we use for our studies in Chapter 3, we measure the 2×2 impedance matrix between port 1 and port 2 from 0.1 GHz to 2.1 GHz. The location of port 1 and the four locations of port 2 are illustrated in Fig. 4.7. The location of port 2 changes for each of the four measurements of the impedance while the location of port 1 remains the same. The port at each of the locations is a 26 cm long low-loss monopole antenna connected to a coaxial cable. The coaxial cable is removed from the impedance measurement through calibration. A mode stirrer rotates a full revolution in increments of 7.2 degrees for a total 50 cavity realizations. The ratio

of the characteristic length of the mode stirrer (cube root of the swept volume) to the characteristic length of the cavity is equal to 0.25.

At high enough frequencies, we expect the system to have two properties. First, we expect that as the stirrer is turned there are a high number of uncorrelated cavity realizations. At a frequency where the cavity is overmoded and the geometry is such that the fields are sensitive to changes to the stirrer position, we expect to generate an large ensemble of uncorrelated measurements and thus a large number of cavity realizations as shown in previous tests of the RCM [46]. The second property of the system has to do with the distribution of the normalized impedances. We expect the distribution to be invariant to the location of port 2. This is due to the assumption that waves ergodically fill the enclosure.

4.3.1 Comparing Normalized Impedance Distributions at Multiple Locations

To find the frequency above which this distribution is invariant to the port location, we normalize the measured impedance using the two-port random coupling model equation,

$$\mathbf{z} = \mathbf{R}_{\mathbf{rad}}^{-\mathbf{1/2}} \left(\mathbf{Z}_{\mathbf{cav}} - \mathbf{j}\mathbf{X}_{\mathbf{rad}} \right) \mathbf{R}_{\mathbf{rad}}^{-\mathbf{1/2}}, \tag{4.9}$$

where $\boldsymbol{Z_{cav}}$ is the measured impedance, $\boldsymbol{R_{rad}}$ and $\boldsymbol{X_{rad}}$ are real and imaginary parts of the radiation impedance. The radiation impedance can be measured using the time gating method as described in Chapter 2. It can also be approximated by averaging $\boldsymbol{Z_{cav}}$ over mode stirrer positions. An example of the radiation impedance

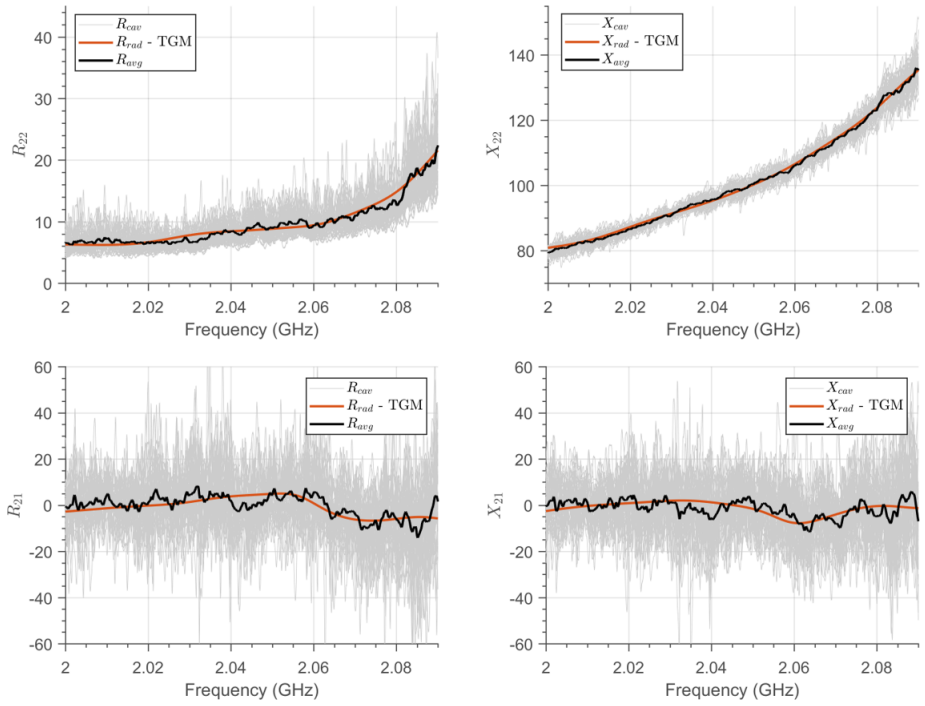

Figure 4.8: An example of the radiation impedance computed from the measured $\boldsymbol{Z_{cav}}$ (gray). The radiation impedance can be computed by the time gating method (TGM) (red) or by averaging $\boldsymbol{Z_{cav}}$ over mode stirrer positions (black).

obtained by both methods is shown in Fig. 4.8. In this section, we use the time gating method to measure the radiation impedance. We then compare the distribution of the normalized impedance at the range of frequencies between 0.1 GHz to 2 GHz. The distributions at high frequencies are shown in Fig. 4.9. The four locations appear to have the same distribution. However, at the lower frequencies as shown in Fig. 4.10, the distributions at the four location appear appear to disagree. For a more quantitative analysis, We then compare the variance of the normalized impedance measured at the four locations. The measured variances of the real and imaginary part of z_{21} and z_{22} is shown in Fig. 4.11. At lower frequencies, the vari-

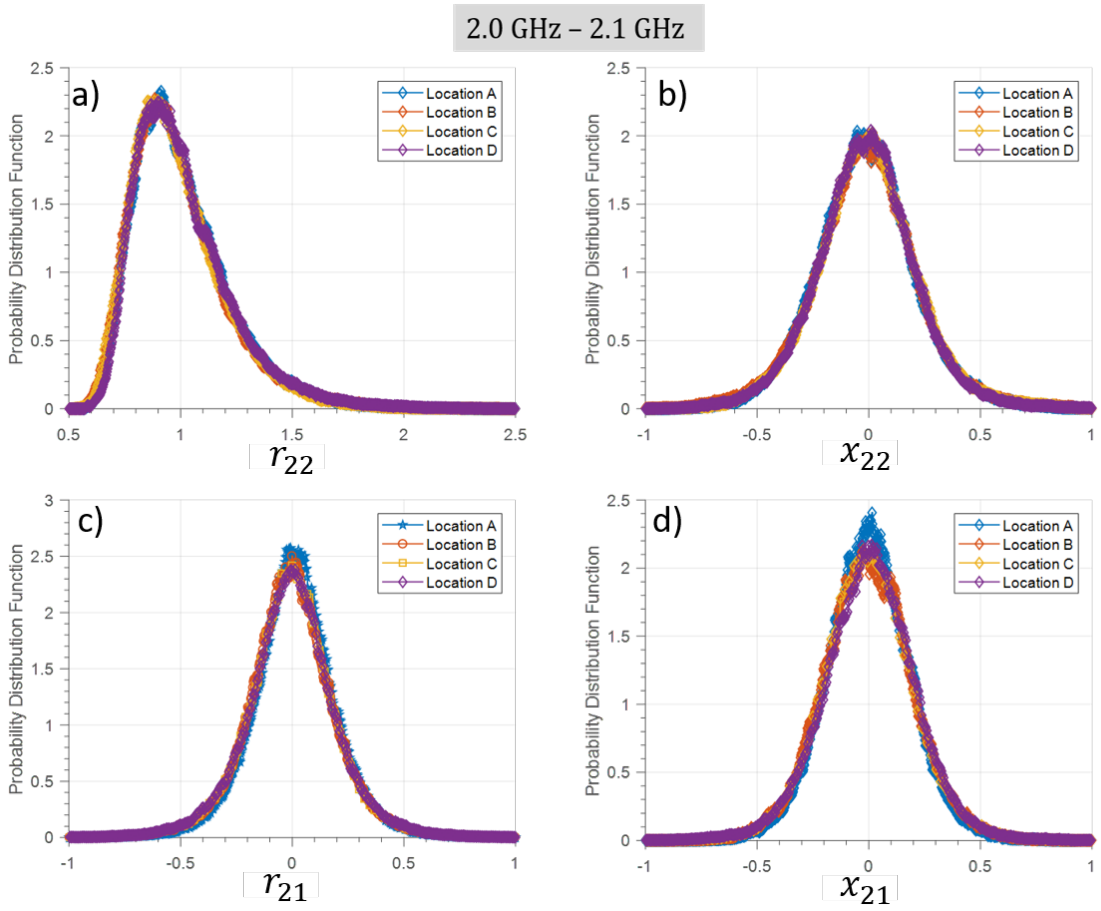

Figure 4.9: The distribution of the normalized impedance between 2 GHz to 2.1 GHz. Shown are the real (a)) and the imaginary part (b)) of $\boldsymbol{z_2 2}$, and the real (c)) and imaginary part (d)) of the $\boldsymbol{z_2 1}$. The distributions of at four locations appear to agree with one another.

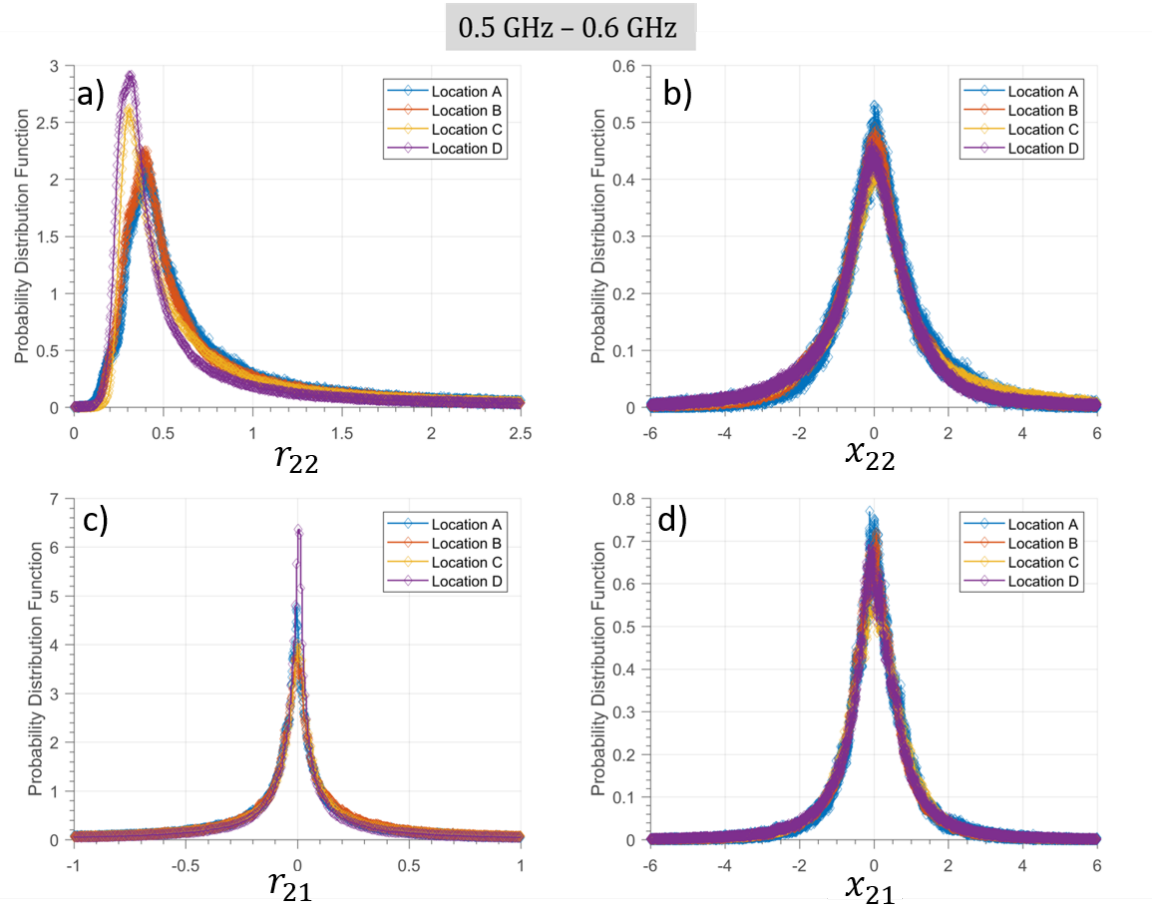

Figure 4.10: The distribution of the normalized impedance between 0.5 GHz to 0.6 GHz. Shown are the real (a)) and the imaginary part (b)) of $\boldsymbol{z_22}$, and the real (c)) and imaginary part (d)) of the $\boldsymbol{z_21}$. The distributions of at four locations, particularly of $\boldsymbol{r_{22}}$ appears to be different for the four locations.

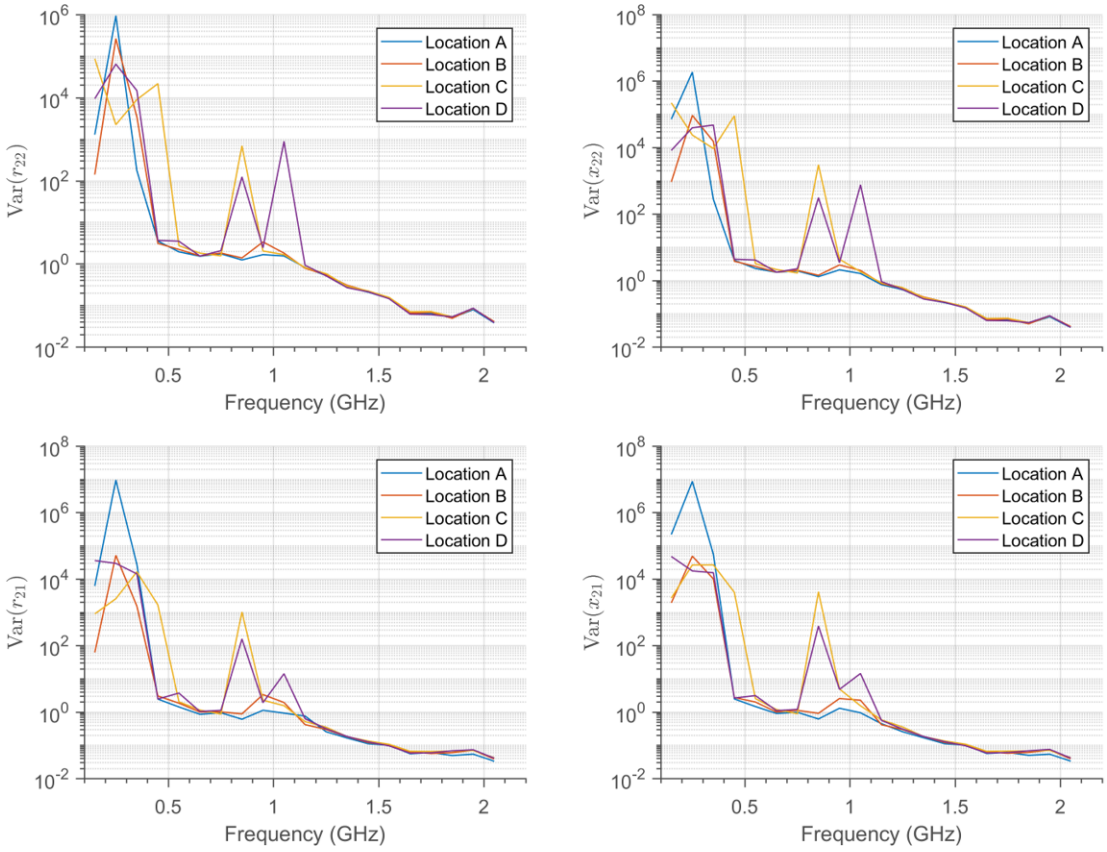

Figure 4.11: The variance of the normalized impedance. At lower frequencies, the variance depends of the location of the port, but at higher frequencies that variance collapses to a single curve

ances are different at the four locations. At these frequencies, the modes are not uniformly stirrer throughout the enclosure. As the mode stirrer rotates, some locations inside the enclosure will see a large variation in the fields and other locations are not as sensitive to the rotation of the stirrer. This presumably arises from a violation of the random plane wave hypothesis of the RCM. However, at frequencies above 1.25 GHz, the variance of the impedance for the four locations collapses to one curve. Therefore, using this as a metric, we would conclude that the lowest usable frequency is 1.25 GHz, which in terms of the ratio of the wavelength to characteristic length (λ/L_{cav}) is 0.2.

4.3.2 The Number of Cavity Realizations as a Metric for the LUF

The other metric for determining the LUF follows from the first property of the mode stirred system described in this section. That is, we expect to find a large number of uncorrelated cavity realizations, N_θ, as the stirrer is turned. The frequency above which a large enough number of cavity realizations are available is deemed to be the LUF. The quantity N_θ is also of interest in the design of reverberation chambers for EMC purposes [47]. The procedure used in that context is also applied here. To determine N_θ, we first compute the Pearson correlation matrix,

$$r_{ij} = \frac{\text{Cov}\left(Z_i, Z_j\right)}{\sqrt{\text{Var}\left(Zi\right)\text{Var}\left(Zj\right)}}(i, j = 0, 1, 2, ..., N), \tag{4.10}$$

where $Z_{i,j}$ is the normalized z_{21} at the i^{th} or j^{th} position and $N = 50$ is the number of cavity realizations. The normalized z_{21} is measured between port 1 and each

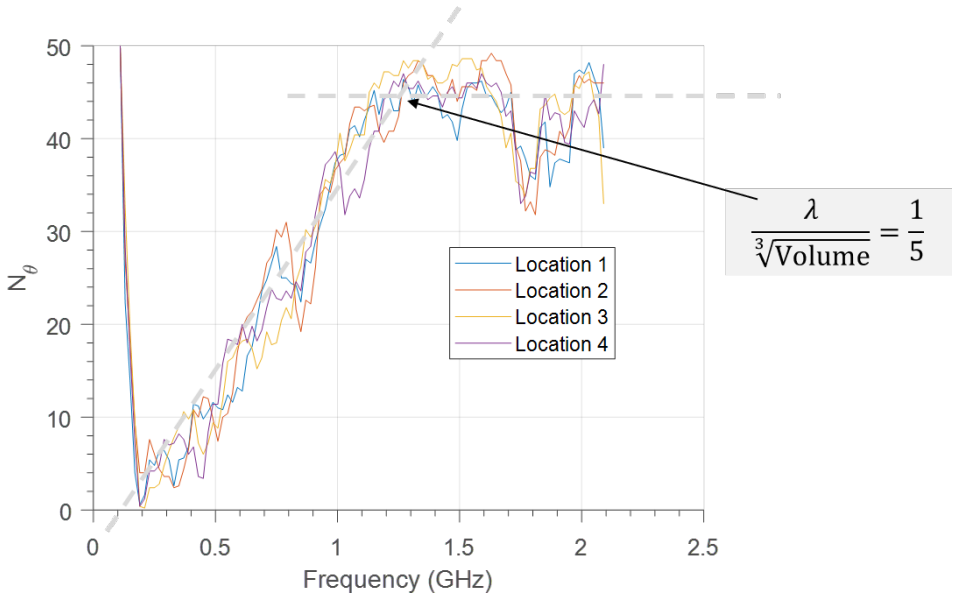

Figure 4.12: The number of uncorrelated positions generated by rotating the mode stirrer, assuming the correlation cutoff $r_s = 0.6$. Note that there are 50 positions in the data set. The data below 0.2 GHz is mostly uncorrelated noise because of a lack of propagating modes

of the port 2 locations. The operators Cov and Var are the covariance and the variance, respectively. After computing the 50×50 matrix, we determine the the number of uncorrelated position for a given correlation threshold r_s as follows. We compute the correlation of all 50 positions to the first position. All the positions with correlation above r_s are removed from the list. Next, the correlation between the second position and all the other positions in the reduced list are computed. Positions with correlation above r_s are again removed. This is repeated for position 3 to 50. The number of positions left in the final list is taken to be the number of uncorrelated positions. Figure 4.12 show the number of uncorrelated positions in our cylindrical enclosure for $r_s = 0.6$. The number seems to reach maximum at around

1.25 GHz for all four positions. At this frequency, the ratio of wavelength to the characteristic length of the cavity is equal to 0.2. Therefore, we use the saturation point of N_θ as a metric for determining the lowest usable frequency of RCM.

4.4 Conclusion

In this chapter, we have illustrated some metrics that can be used to determine the lowest usable frequency (LUF) for the random coupling model. With numerical calculation, we solve for the eigenmodes of a cavity and study the distribution of the fields. The RCM assumes the fields within a region in the cavity have a Gaussian distribution. We use the Kolmogorov-Smirnov test to compare the field distribution to a Gaussian, and to determine the frequency above which the fields are said to be Gaussian distributed and thereby deem the RCM applicable. In 3D enclosures, we measured the variance of the normalized impedance at four different locations within the enclosure. The RCM predicts that the variances are the same. From the variance measurements, we can identify the frequency above which the variances are consistently the same at all four locations. Finally, we measured the number of independent positions generated by the rotation of the mode stirrer. For a given correlation threshold, we compute the number of uncorrelated measurements. We can use the frequency above which the number of uncorrelated measurements saturate as a metric to determine the LUF. From the various metrics discussed in the chapter, we gather that the LUF in term of the ratio of the wavelength to characteristic length of the cavity ($\lambda/V^{1/3}$) to be in the range of 0.2 to 0.35.

Chapter 5: Microwave Analog to Chaotic Regularization of Quantum Tunneling Rates

In this chapter, we will use the methods and tools of microwave systems to experimentally validate a quantum mechanical concept. Specifically, we study chaos regularization of tunneling rates, the theory of which is presented in [48, 49]. In the microwave analog, we demonstrate this principle through simulations in full wave computational electromagnetic software and physical experiments in superconducting microwave cavities. Both are presented in this chapter.

5.1 Introduction

We consider a mirror symmetric double well systems separated by tunneling barrier as shown in the insets of Fig. 5.1 and discussed in [48]. In this quantum mechanical problem, the potential energy inside the wells is equal to 0, the potential in the tunneling barrier region is equal to $V_B > E$, where V_B is a constant, E is the energy of the eigenstates, and the potential is equal to infinity elsewhere. The eigenstates have even and odd parity with respect to center. The presence of the tunneling barrier causes a splitting of the energy of the eigenstates, with the energies of the symmetric eigenstates E_s being slightly smaller than the energies of

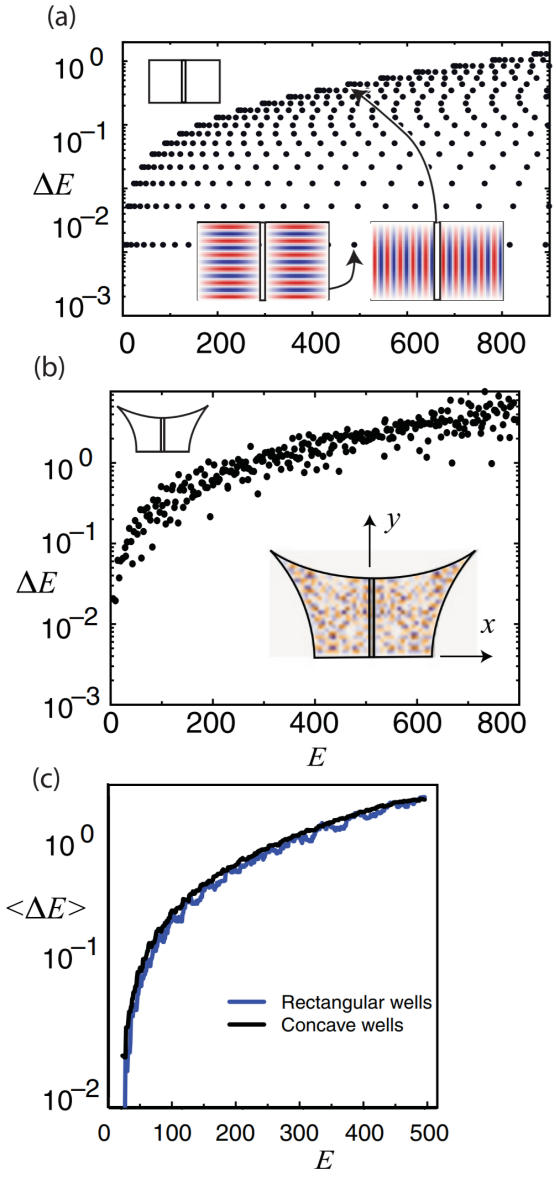

Figure 5.1: The tunneling rates in integrable (a) and chaotic cavities (b). The fluctuation of the tunneling rates is much higher in the integrable case, but the sliding average (c) is independent of the shape of the cavity. This result presented by Pecora et. al in [48] and reprinted here with the permission of American Physical Society.

the antisymmetric states E_a [49]. The difference, $\Delta E = E_a - E_s$, is referred to as the tunneling rate.

There were two main results presented by Pecora et. al [48]. The first result is that fluctuations in the tunneling rate are much larger for integrable cavities compared with those of chaotic cavities. This is because the tunneling rate is a function of the incident angle of a ray at the barrier. In the chaotic cavity, by the random plane wave hypothesis as discussed in Sec. 4.1, the propagation angles are uniformly distributed in $[0, 2\pi)$. However, in the integrable cavity the incident angles are restricted and differ from mode to mode. Waves with incident angles that are nearly tangential to the barrier will tunnel less than those with angles nearly perpendicular as shown in the inset of Fig. 5.1(a). The second result predicted in [48] is that the sliding average of the tunneling rate will be independent of the cavity shape given the same cavity area and the same tunneling barrier. This is demonstrated in the result shown in Fig. 5.1(c).

In order to experimentally validate the theoretical results from [48], we look to microwave cavities. The probability amplitude of a quantum mechanical particle has an analog in the transverse electric field of a thin two-dimensional microwave cavity. The "tunneling barrier" for the microwave cavity as shown in Fig. 5.2 is due to the septa forming a series of the waveguides with cutoff frequencies below the range of frequencies we study.

The Schrodinger Equation can be written as the wave equation in the Helmholtz form,

$$\left(\nabla^2 + k^2\right) \phi\left(\mathbf{x}\right) = 0, \tag{5.1}$$

where $\phi(\mathbf{x})$ is the wave field as a function of position $\mathbf{x}$ and k is the wavenumber. For a quantum mechanical system, $k^2 = E - V_b$, but for the transverse electric wave in the microwave system $k^2 = K^2 - K_b^2$ where $K_b^2 = 0$ in the cavity and K_b^2 in the septa is approximated by the square of the cutoff wavenumber of the waveguides in the septa, and is given by

$$K_b^2 = \frac{\pi^2}{d^2} \tag{5.2}$$

where d is the separation distance between the waveguide plates (see Fig. 5.2). Therefore, the energy states of the quantum mechanical particle, E, have an analog in the squared eigenfrequencies, $F_n \equiv f_n^2$, of the microwave system. Similarly, the energy splitting or tunneling rate, ΔE, has an analog in the splittings of the squared microwave eigenfrequencies, Δf^2.

The remainder of this chapter is organized as follows. In Section 5.2, we will present and discuss simulation results of the frequencies splittings in integrable and chaotic microwave cavities. In Section 5.3, experimental results of the superconducting cavities are presented. In Section 5.4, the results of this chapter are summarize and suggestions for future projects is presented.

5.2 Simulation of the Tunneling Rates in Cavities

A rectangular cavity and a bowtie shaped cavity are modeled in Ansoft HFSS [36]. The geometry and dimensions of the rectangular cavity are shown in Fig. 5.2. In both cavities, the dimensions of the septa as well as the area of the cavities is the same. The curved boundaries of the bowtie cavity is constructed by two identical

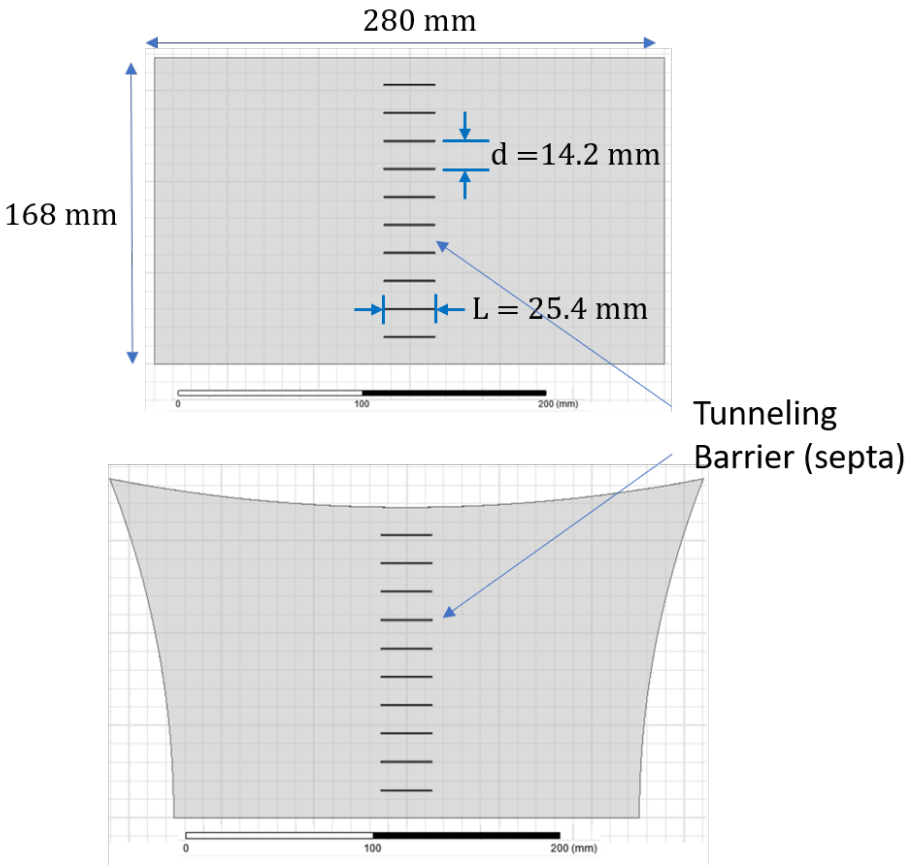

Figure 5.2: The microwave cavities used to study the tunneling rates in HFSS. Both the integrable (a) and the chaotic (b) cavities have the same area and the same "tunneling barrier"

circles on the sides of radius 504 mm with larger circle at the top of radius 840 mm. The bottom surface is kept flat. The location of the circles on the sides are moved to match the area of rectangular cavity. The height of the cavities in the third dimension is 2.5 mm, which means as long as we measure below the 60 GHz cut-off frequency, the field solutions will be essentially two dimensional. The separation, d, between the septa is 14.2 mm; therefore, by Eq. 5.2, the cutoff wavenumber is $K_b = 221.2\ m^{-1}$ and the cutoff frequency is $f_b = \frac{K_b c}{2\pi} = 10.6$ GHz.

Using HFSS, we compute the first 60 eigenfrequencies above 2 GHz in the cavity, which as a result of the septa come in split pairs. We compute the difference between the squared eigenfrequencies. The splitting of the squared eigenfrequencies is Δf^2. The difference from one pair of squared eigenfrequencies to the next is ΔF^2. The relationship between ΔF^2 and Δf^2 is shown in Fig. 5.3. The quantities ΔF^2 and Δf^2 computed from a table of eigenfrequencies are shown in Fig. 5.4.

From the simulation, we can determine the mean mode spacing ΔK^2 which is directly proportional to the ΔF^2. The moving average of ΔF^2 appears to be constant, independent of frequency for both the chaotic and integrable cavities. This is expected because for a 2D cavity the spacing between adjacent cavity modes ($\Delta K^2 = K_{n+1}^2 - K_n^2$) as predicted by Weyl formula is frequency independent [20], and given by

$$\Delta K^2 = \frac{4\pi}{A} \tag{5.3}$$

where A is the area of the cavity on one side of the septa.

More importantly, the frequency splitting or the spacing between symmetric

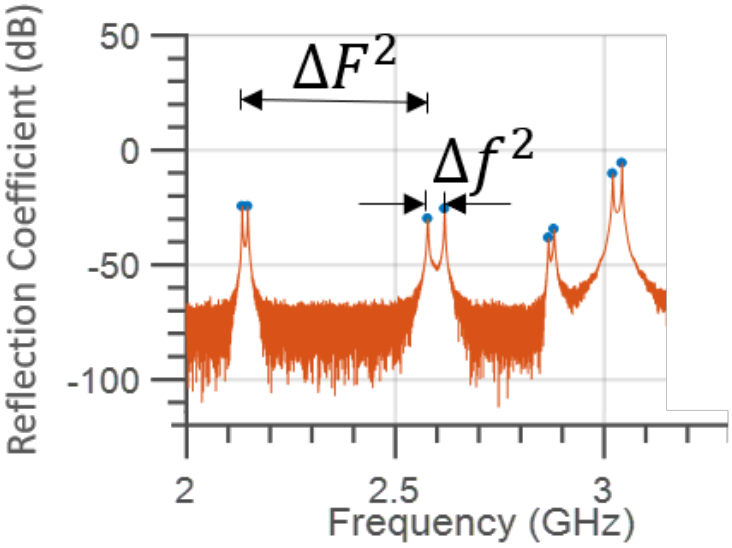

Figure 5.3: An illustration of Δf^2 and ΔF^2 shown in a prospective measurement of the reflection coefficient at port inside the cavity.

and antisymmetric modes, Δf^2, which we have referred to as the tunneling rate, increases with frequency. This is because as the frequency approaches that of the cutoff waveguide in the septa region more of the energy travels through evanescent waves to the adjacent cavity. The moving average of Δf^2 as shown in Fig. 5.5 appears to be the same in both cavities as predicted in [48]. Additionally, we observe a reduction in the fluctuations of the tunneling rate in the bowtie cavity compared to the rectangular cavity. The fluctuations about the moving average is computed to be roughly 25% smaller for the bowtie cavity. Therefore, we have numerically demonstrated regularization of tunneling rates in chaotic cavities.

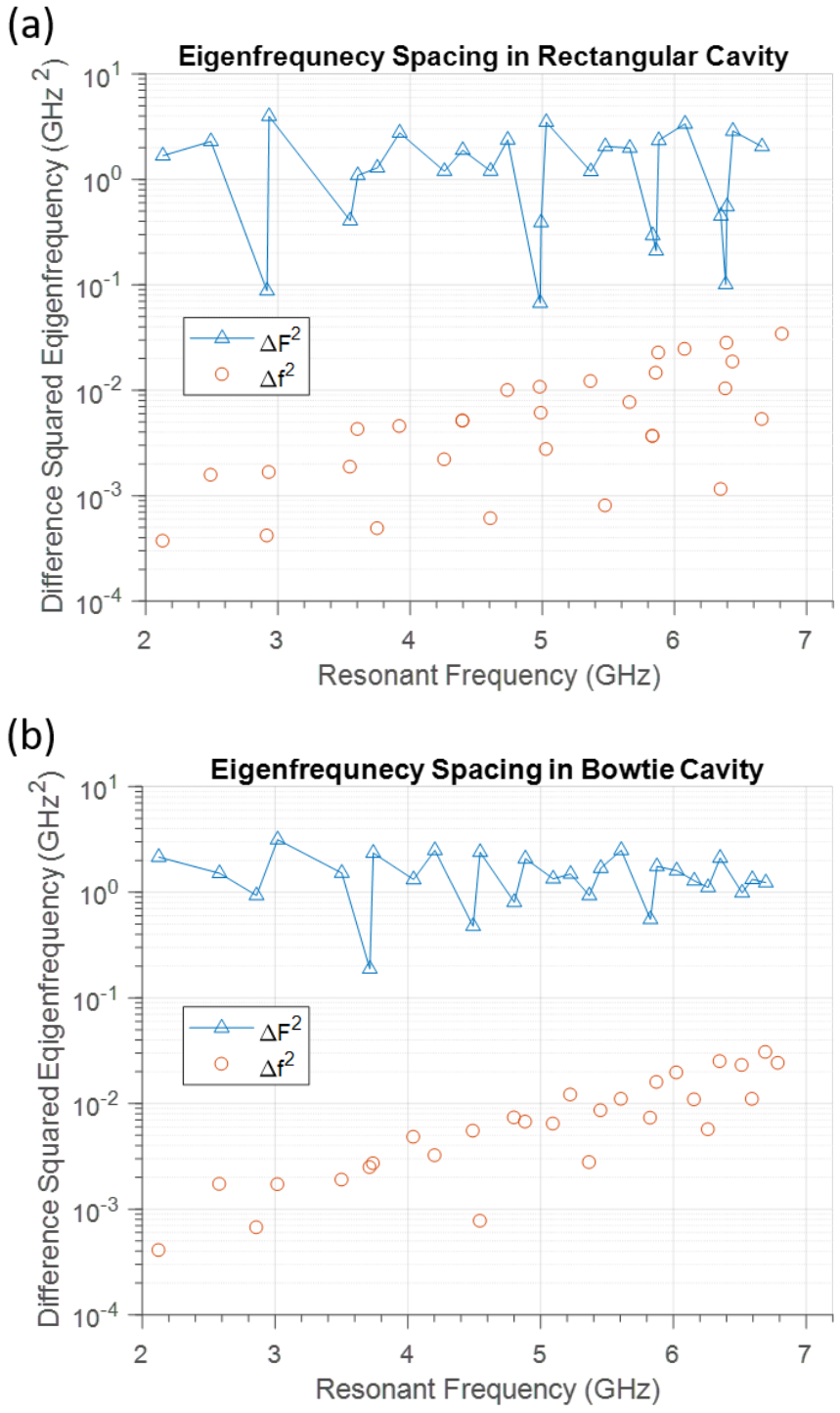

Figure 5.4: The difference in the square of the eigenfrequencies for the rectangular (a) and the bowtie (b) cavity. As the eigenfrequencies split pair come in pairs, the difference within the pair is Δf^2 and the difference from one set to another is ΔF^2

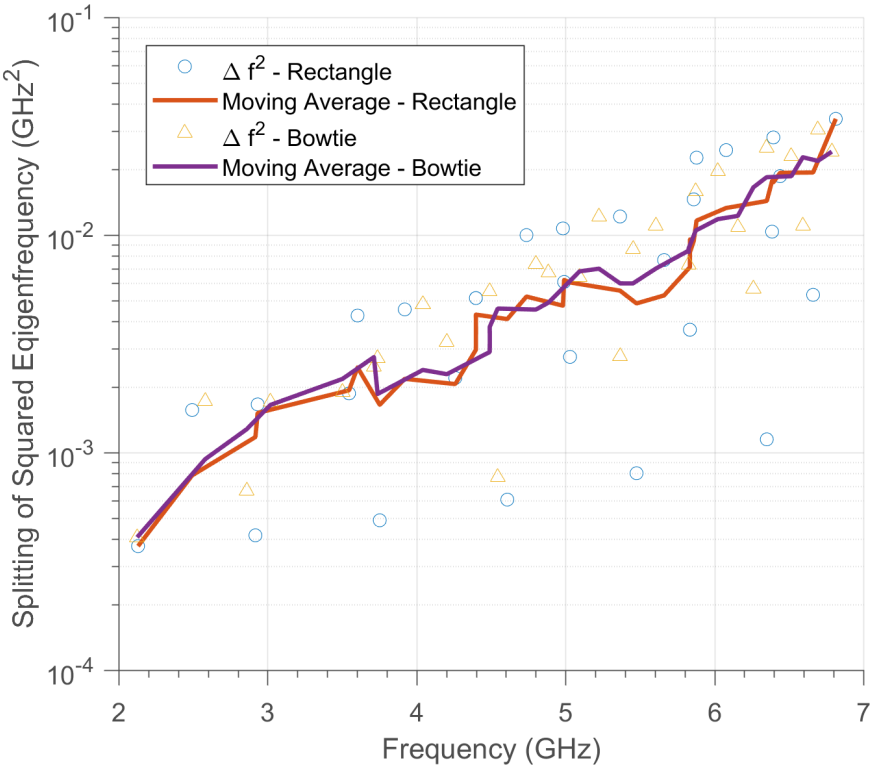

Figure 5.5: The frequency splitting in the rectangular and bowtie cavities. The moving average of appear to be the same in both cavities while the fluctuation is smaller for the bowtie cavity

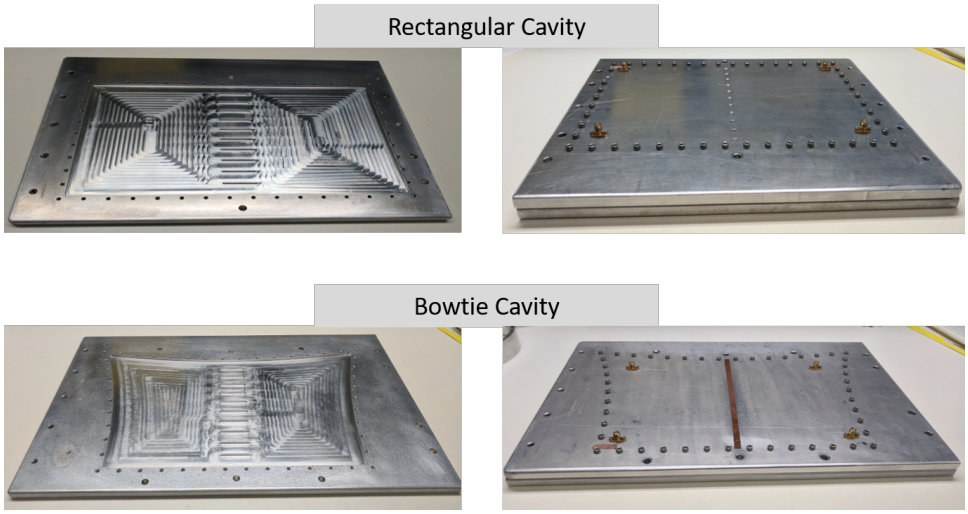

Figure 5.6: The quasi-2D aluminum cavities used to study the tunneling rates. Both sides of the rectangular and bowtie cavities are carved a depth of 2.5 mm and have the same area and the same "tunneling barrier" The left images show the milled bottom plate. The right images show the lid attached to the bottom plate.

5.3 Experiments in Superconducting Microwave Cavities

For the purpose of experimental validation of chaos regularization of tunneling rates, the cavities simulated in Section 5.2 are designed and built by Rachel Owen and John Rodgers [50]. Two cavities of depth of 2.5 mm in the shape of the two simulated cavities including the septa were milled in bulk of 6061 alloy aluminum. This is shown in Fig. 5.6. Another aluminum plate is screwed on top to form the cavity. On either side of the septa, coaxial fed ports were added with the center pin extruding about half way into the cavity.

The cavities were cooled in a dilution refrigerator shown in Fig. 5.7 to about 100 mK. This temperature is much lower than the critical temperature for supercon-

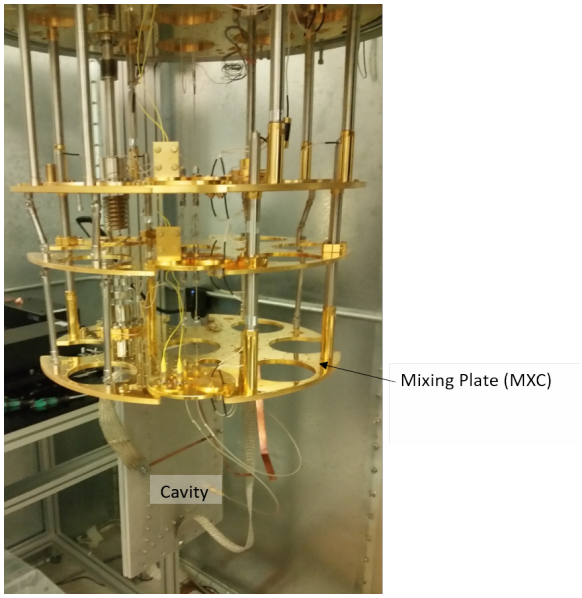

Figure 5.7: The aluminum cavity mounted in the dilution refrigerator. The chamber is closed and cooled to about 100 mK.

ductivity of about 1 K for the 6061 aluminum alloy [51]. We placed a thermometer at the bottom of the cavity as well as at the coldest point in the dilution refrigerator, the mixing plate (MXC) shown in Fig. 5.7. The temperature profile as a function of time is shown in Fig. 5.8. The temperature on the MXC is lower than on the cavity itself; however we were able to reach below 100 mK on the cavity. The oscillations in the temperature are due to the act of radiating into the cavity for the purpose measuring the transmission coefficient.

We measured the transmission coefficient from one side of the septa to the other in a network analyzer. The experimental setup for this measurement is shown in Fig. 5.9. The superconductivity of the aluminum increases the quality factor by about fivefold compared to the cavity at room temperature. This improves our

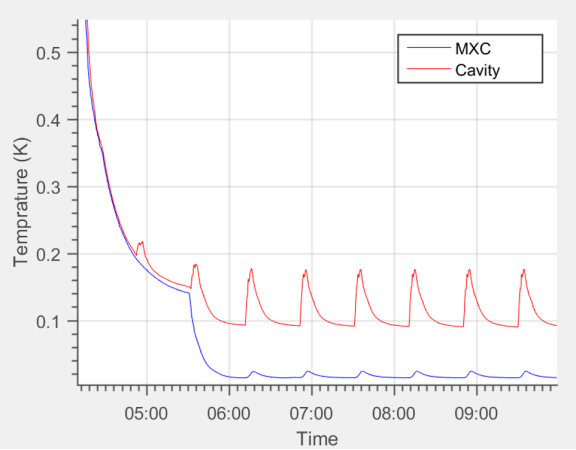

Figure 5.8: The temperature profile of the cavity in the dilution refrigerator. The temperature at mixing plate and the cavity are shown over a six hour period.

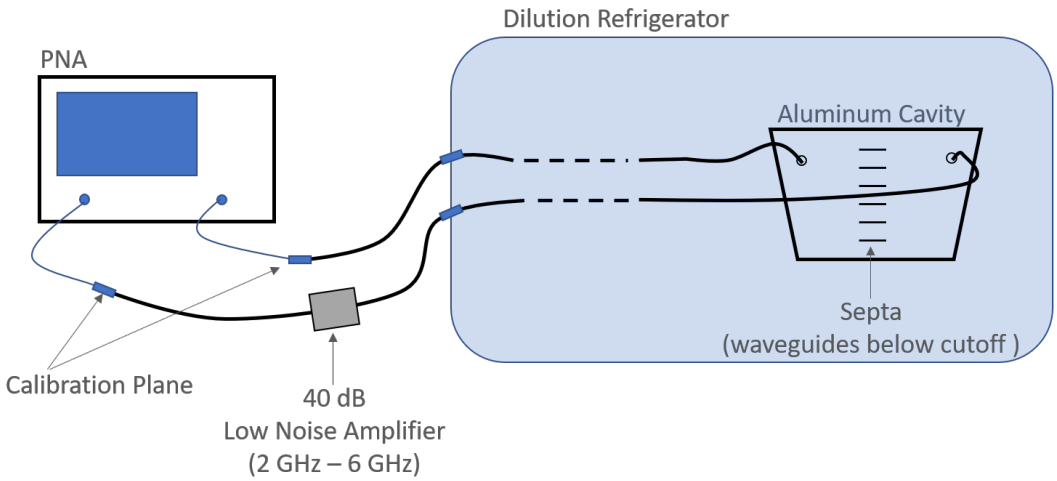

Figure 5.9: The experimental setup for measuring the transmission coefficient in the cavities

ability to identify the narrow frequency splittings in the transmission coefficient measurement. However, at higher frequencies where Q-widths are greater than the frequency splitting, the symmetric/antisymmetric modes overlap and we have difficulties identifying the frequency splittings. Even though we have removed ohmic loss in the walls, which was the dominant contributor to the the quality factor, there are other loss mechanism, as discussed in Sec. 3.2 by which the power from the cavity can still dissipate including leakage through seams in the cavity as well as through the ports. This limits the quality factor.

The measured transmission coefficient, S_{21} for the bowtie cavity is shown in Fig. 5.10. The resonant peaks are identified using the `findpeaks.m` function in MATLAB [52]. At lower frequencies, the peaks and the frequency splitting are clearly identified. However, at higher frequencies the Q-widths of the resonances are on the order of the frequency splitting which results in misidentifying superposition of two very close resonant peaks as a single peak.

We have also measured the transmission coefficient in the rectangular cavity. However as demonstrated in Sec. 5.2, the tunneling rates are not regularized in the rectangular cavity, so the frequency splitting can take a wide range of values including very small splittings at lower frequencies. This can be seen in Fig. 5.11. Beginning with first resonance above 2 GHz, the Q-widths are not small enough to resolve the frequency splitting. The fact that we were able to identify the splitting more easily with bowtie cavity indicates chaos regularization of the tunneling rates. However, in order to fully validate this principle a much higher quality factor cavity is required. Some suggestions for increasing the quality factor are presented in the

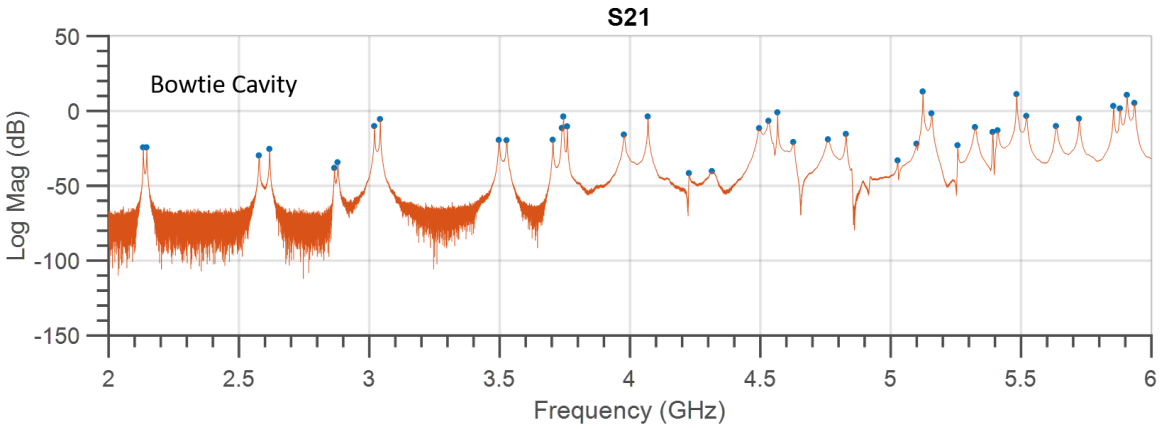

Figure 5.10: The measured S_{21} for the bowtie cavity. The blue dots indicate the location of the identified peaks.

next section.

5.4 Conclusion

In this chapter we have demonstrated in the HFSS simulations that the fluctuations of the tunneling rates are much higher between two rectangular cavities than between two bowtie cavities. This is the microwave analog to quantum chaos regularization of the tunneling rates presented in [48]. In order to experimentally demonstrate this phenomenon, we need to be able to identify very close resonant peaks in the transmission coefficient, which we found requires the quality factor to be higher such that the Q-width is much smaller than the smallest frequency splitting. There are a couple of ways to achieve sufficiently higher quality factor that we could explore in the future. One suggestion is to increase the depth of the cavities. This will increase the volume and in effect increase the stored energy. The quality

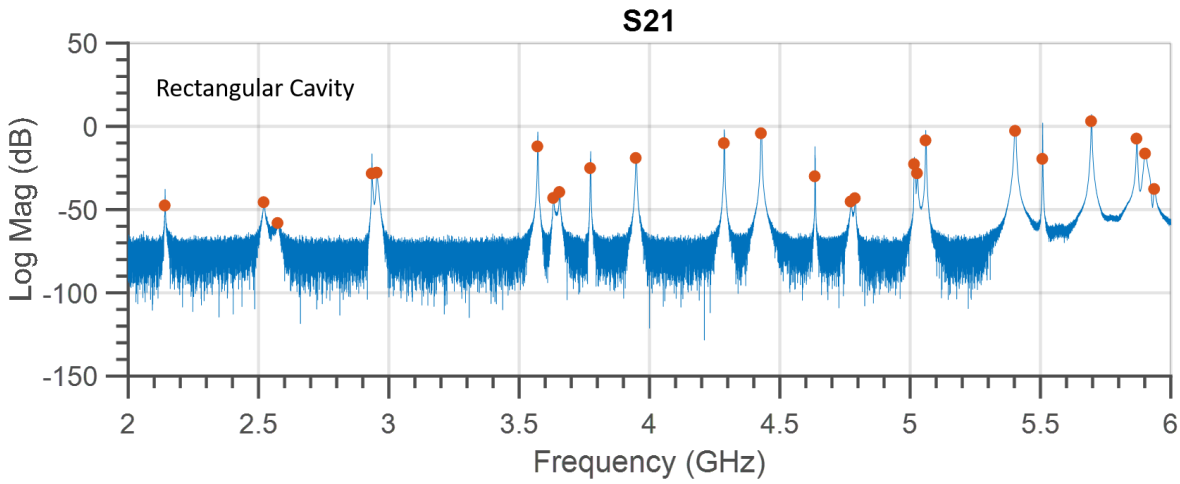

Figure 5.11: The measured S_{21} for the bowtie cavity. The red dots indicate the location of the identified peaks.

factor, defined by Eq. 3.1, is directly proportional to the stored energy and will increase accordingly. The depth of the cavity used for this project can be increased to the separation width of the waveguides in the septa while maintaining 2D solutions of the wave equation. Another suggestion would be to minimize any leakage in the cavity. The cavity is formed by joining two aluminum plates using 50 screws around the perimeter of the cavities. With the changing temperatures of the cavities placed in the dilution refrigerator, the aluminum will expand and contract which may allow EM energy to leak. If we could eliminate this possibility for leakage, we could increase the quality factor, which will allow us experimentally validate chaos regularization of the tunneling rates.

Chapter 6: Final Conclusion and Future Work

Modeling the wave propagation in complex enclosures with multiple ports is of interest to many disciplines. In this dissertation, we studied the statistics of the scattering and impedance parameters in complex electromagnetic enclosures. A focus point for this dissertation has been the random coupling model (RCM). The RCM has been successfully demonstrated as a statistical model to characterize the impedance matrix of multi-port complex electromagnetic enclosures. [22]. However, there are some challenges to implementing the RCM in practical systems, which have been addressed in this dissertation.

One of these challenges is measuring the radiation impedance, Z_{rad}. In Chapter 2, the time gating method is introduced as a method to measure Z_{rad}. Along with the loss parameter, the radiation impedance is one of the system-specific parameters required to form the RCM. In previous tests of the RCM, the radiation impedance has been measured by covering the enclosure walls with absorbers to dampen the reflections from the enclosure. However, lining the enclosure with absorber can be prohibitively time consuming. In some cases, we may not have access to the parts of the enclosure. We could alternatively simulate the port; however, this does require that we know the exact dimensions and materials of the port, of which we may

not have access. The time gating method, measures the radiation impedance in a non-intrusive way by suppressing portions of the time domain measurement larger than the gating time.

Another challenge addressed in this dissertation is localized loss at the ports of complex enclosures. Under the condition of a lossy port, the radiation impedance at the port is difficult to measure by any method including the time gating method. However, in Chapter 3, we show that if the enclosure is also lossy, the impedance statistics can still be characterized using a modified RCM formulation. The new formulation is derived where the radiation efficiency of the port is an additional parameter required to characterize the system. This models is successfully tested on an antenna with significant dielectric loss at the port.

In addition to addressing these challenges of implementing RCM, we discuss methods to determine the lowest usable frequency of the RCM. The key assumptions of the RCM which are an overmoded enclosure and the the random plane wave hypothesis break down at lower frequencies. Some methods to measured this break down is discussed in Chapter 4. The LUF is given in terms of the ratio of the wavelength to the characteristic length of the enclosure which we found to be between 0.2 to 0.35.

Finally in Chapter 5, we demonstrate the quantum mechanical principle of chaos regularization of tunneling rates in cavities [48]. The mirror symmetric double well system with a tunneling barrier has an analog case in microwave systems, which we demonstrated in this chapter. Although, the RCM was not a subject of this chapter, we used the concept of the random plane wave hypothesis and the tools of

microwave systems to demonstrate the principle.

The RCM has been a topic of several dissertation at the University of Maryland [12, 20, 53, 54, 54]; however, there are still some future work that can be done to fully test the RCM. One of these projects is to study broken-time-reversal-symmetric (BTRS) systems. The RCM theory can handle BTRS systems, but the experimental tests of the RCM in 3D enclosures presented here and in previous projects have been time-reversal-symmetric systems. Using large magnetized ferrites materials in enclosures, we could test BTRS systems as well. Another project that is more directly related to this dissertation is to generalize the lossy port formalism discussed in Chapter 3 to low loss cavities ($\alpha < 1$). We were able to avoid computing the three unknown impedances in Fig. 3.3 by applying the radiation efficiency parameter. However, the assumptions leading to the new RCM formulation are only applicable to lossy cavities. For moderate to low-loss cavities with lossy ports, a new method is required.

Appendix A: Determining the Minimum Rotation Step of the Mode Stirrer

In order to study the impedance statistics in the complex enclosures, we need to collect a large ensemble of measurements. The mode stirrer in the enclosure allows us to obtain many cavity realizations. Inside the cylindrical enclosure discussed in Chapter 3 (see Fig. 3.5), the mode stirrer is an aluminum sheet 18.5 cm X 48 cm suspended on a rod from the top of the cylinder at 45 degree angle as shown in Fig. A.1. To obtain a new cavity realization, the rod is rotated by small angular step. However, unless the step size is large enough, the new measurement will be strongly correlated to previous measurement. This means the new measurement does not add new data to the ensemble. This could even skew the statistics. Therefore, we need to determine the angle step size above which adjacent measurements are minimally correlated.

In order to study the correlation between consecutive measurements, we compute the Pearson correlation coefficient matrix using the following procedure. We measure the reflection coefficient, S_{11}, in the frequency range of interest for 200 positions of the mode stirrer. Each mode stirrer position is separated by an angle $\theta = 1.8$ degrees from an adjacent position. Then, we compute the elements of the

Figure A.1: The mode stirrer inside the cylindrical enclosure

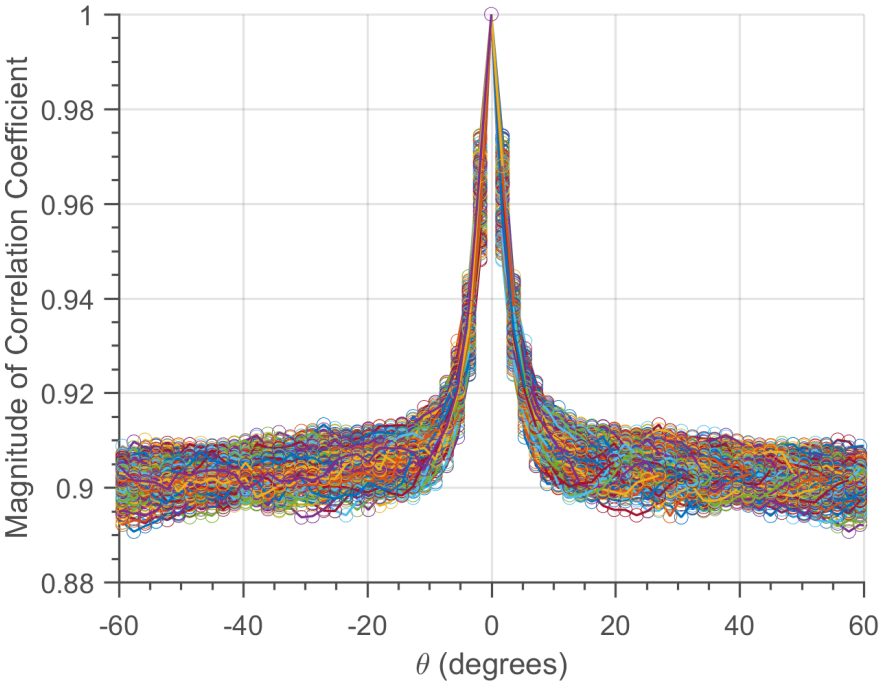

Figure A.2: The columns of Pearson correlation coefficient matrix for S_{11} measurements across 200 mode stirrer positions separated by an angle θ away from each other

Pearson correlation coefficient matrix given by

$$\rho\left(i,j\right)=\frac{\mathrm{Cov}\left(S_i,S_j\right))}{\sqrt{\mathrm{Var}\left(S_i\right)\mathrm{Var}\left(S_j\right)}} \tag{A.1}$$

where $S_{i,j}$ is the measured S_{11} for the location indices i or j ranging from 1 to 200, Cov and Var are the covariance and variance operators, respectively.

The columns of the correlation coefficient are shown Fig. A.2. The measurements becomes minimally correlated if we rotate the mode stirrer by about 7 degrees or more. Therefore, for the measurements reported in Chapter 3 and Chapter 4, we measure at 50 mode stirrer positions each separated by 7.2 degrees from a neighboring position.

Bibliography

[1] Richard Holland. *Statistical Electromagnetics*. CRC Press, 1st edition, November 1999.

[2] R. H. Price, H. T. Davis, and E. P. Wenaas. Determination of the statistical distribution of electromagnetic-field amplitudes in complex cavities. *Phys. Rev. E*, 48:4716–4729, Dec 1993.

[3] H.-J. Stöckmann and J. Stein. Quantum chaos in billiards studied by microwave absorption. *Phys. Rev. Lett.*, 64:2215–2218, May 1990.

[4] Y. Alhassid. The statistical theory of quantum dots. *Rev. Mod. Phys.*, 72:895–968, Oct 2000.

[5] Yves Aurgan and Vincent Pagneux. Acoustic scattering in duct with a chaotic cavity. *Acta Acustica united with Acustica*, 102(5):869875, Jan 2016.

[6] R. L. Weaver. Spectral statistics in elastodynamics. *The Journal of the Acoustical Society of America*, 85(3):10051013, 1989.

[7] C. Ellegaard, T. Guhr, K. Lindemann, H. Q. Lorensen, J. Nygård, and M. Oxborrow. Spectral statistics of acoustic resonances in aluminum blocks. *Phys. Rev. Lett.*, 75:1546–1549, Aug 1995.

[8] G.B. Tait and M.B. Slocum. Electromagnetic environment characterization of below-deck spaces in ships. In *Electromagnetic Compatibility, 2008. EMC 2008. IEEE International Symposium on*, pages 1–6, Aug 2008.

[9] D.M. Johnson, M.O. Hatfield, and G.J. Preyer. Rf coupling measurements on passenger aircraft avionics exposed to cavity-mode excitation. In *Digital Avionics Systems Conference, 1995., 14th DASC*, pages 427–432, Nov 1995.

[10] Xing Zheng, Thomas M. Antonsen Jr, and Edward Ott. Statistics of impedance and scattering matrices in chaotic microwave cavities: Single channel case. *Electromagnetics*, 26(1):3–35, 2006.

[11] Xing Zheng, Thomas M. Antonsen, and Edward Ott. Statistics of impedance and scattering matrices of chaotic microwave cavities with multiple ports. *Electromagnetics*, 26(1):37–55, 2006.

[12] Sameer Dileep Hemmady. *A Wave-Chaotic Approach To Predicting And Measuring Electromagnetic Field Quantities In Complicated Enclosures*. PhD thesis, University of Maryland, College Park, MD, 10 2006.

[13] L. K. Warne, K. S. H. Lee, H. G. Hudson, W. A. Johnson, R. E. Jorgenson, and S. L. Stronach. Statistical properties of linear antenna impedance in an electrically large cavity. *IEEE Transactions on Antennas and Propagation*, 51(5):978–992, May 2003.

[14] Robert E Richardson. Reverberant microwave propagation. Technical report, DTIC Document, 2008.

[15] G. Tait, M. Slocum, and R. Richardson. On multipath propagation in electrically large reflective spaces. *Antennas and Wireless Propagation Letters, IEEE*, 8:232–235, 2009.

[16] Eugene P Wigner. On a class of analytic functions from the quantum theory of collisions. In *The Collected Works of Eugene Paul Wigner*, pages 409–440. Springer, 1993.

[17] Edward Ott. *Chaos in dynamical systems*. Cambridge university press, 2002.

[18] Hans-Jürgen Stöckmann. *Quantum chaos: an introduction*. Cambridge university press, 2006.

[19] S. Deus, P. M. Koch, and L. Sirko. Statistical properties of the eigenfrequency distribution of three-dimensional microwave cavities. *Phys. Rev. E*, 52:1146–1155, Jul 1995.

[20] X. Zheng. *Statistics of impedance and scattering matrices in chaotic microwave cavities: The random coupling model*. PhD thesis, University of Maryland, College Park, 2005.

[21] Gabriele Gradoni, Jen-Hao Yeh, Bo Xiao, Thomas M. Antonsen, Steven M. Anlage, and Edward Ott. Predicting the statistics of wave transport through chaotic cavities by the random coupling model: A review and recent progress. *Wave Motion*, 51(4):606 – 621, 2014. Innovations in Wave Modelling.

[22] S. Hemmady, T.M. Antonsen, E. Ott, and S.M. Anlage. Statistical prediction and measurement of induced voltages on components within complicated enclosures: A wave-chaotic approach. *Electromagnetic Compatibility, IEEE Transactions on*, 54(4):758–771, Aug 2012.

[23] Sameer Hemmady, Xing Zheng, Edward Ott, Thomas M. Antonsen, and Steven M. Anlage. Universal impedance fluctuations in wave chaotic systems. *Phys. Rev. Lett.*, 94:014102, Jan 2005.

[24] P. W. Brouwer and C. W. J. Beenakker. Voltage-probe and imaginary-potential models for dephasing in a chaotic quantum dot. *Phys. Rev. B*, 55:4695–4702, Feb 1997.

[25] C. W. J. Beenakker. Random-matrix theory of quantum transport. *Rev. Mod. Phys.*, 69:731–808, Jul 1997.

[26] Y. Alhassid. The statistical theory of quantum dots. *Rev. Mod. Phys.*, 72:895–968, Oct 2000.

[27] M. L. Mehta. *Random Matrices (Pure and applied mathematics, v. 142)*. Elsevier Science Limited, 2004.

[28] G. Burrell and A. Jamieson. Antenna radiation pattern measurement using time-to-frequency transformation (tft) techniques. *IEEE Transactions on Antennas and Propagation*, 21(5):702–704, Sep 1973.

[29] P. Gonzlez-Blanco and M. Sierra-Castaer. Time filtering techniques for echo reduction in antenna measurements. In *2016 10th European Conference on Antennas and Propagation (EuCAP)*, pages 1–3, April 2016.

[30] J. Tian, L. Zhang, N. Li, and W. Chen. Time-gating method for v/uhf antenna pattern measurement inside an anechoic chamber. In *2008 International Conference on Microwave and Millimeter Wave Technology*, volume 2, pages 942–945, April 2008.

[31] Q. Xu, Y. Huang, L. Xing, Z. Tian, M. Stanley, and S. Yuan. B-scan in a reverberation chamber. *IEEE Transactions on Antennas and Propagation*, 64(5):1740–1750, May 2016.

[32] Jen-Hao Yeh, James A. Hart, Elliott Bradshaw, Thomas M. Antonsen, Edward Ott, and Steven M. Anlage. Universal and nonuniversal properties of wave-chaotic scattering systems. *Phys. Rev. E*, 81:025201, Feb 2010.

[33] J. A. Hart, T. M. Antonsen, and E. Ott. Effect of short ray trajectories on the scattering statistics of wave chaotic systems. *Phys. Rev. E*, 80:041109, Oct 2009.

[34] K. Lu and T. J. Brazil. A systematic error analysis of hp 8510 time-domain gating techniques with experimental verification. In *1993 IEEE MTT-S International Microwave Symposium Digest*, pages 1259–1262 vol.3, June 1993.

[35] B. D. Addissie, J. C. Rodgers, and T. M. Antonsen. Application of the random coupling model to lossy ports in complex enclosures. In *2015 IEEE Metrology for Aerospace (MetroAeroSpace)*, pages 214–219, June 2015.

[36] Ansoft. ANSYS HFSS, 3D Full-wave Electromagnetic Field Simulation.

[37] D. A. Hill. Electromagnetic fields in cavities: Deterministic and statistical theories [advertisement]. *IEEE Antennas and Propagation Magazine*, 56(1):306–306, Feb 2014.

[38] D. A. Hill, M. T. Ma, A. R. Ondrejka, B. F. Riddle, M. L. Crawford, and R. T. Johnk. Aperture excitation of electrically large, lossy cavities. *IEEE Transactions on Electromagnetic Compatibility*, 36(3):169–178, Aug 1994.

[39] J. M. Dunn. Local, high-frequency analysis of the fields in a mode-stirred chamber. *IEEE Transactions on Electromagnetic Compatibility*, 32(1):53–58, Feb 1990.

[40] Fritz Haake, Georg Lenz, Petr Seba, Jürgen Stein, Hans-Jürgen Stöckmann, and Karol Życzkowski. Manifestation of wave chaos in pseudointegrable microwave resonators. *Phys. Rev. A*, 44:R6161–R6164, Nov 1991.

[41] Steven W. McDonald and Allan N. Kaufman. Wave chaos in the stadium: Statistical properties of short-wave solutions of the helmholtz equation. *Phys. Rev. A*, 37:3067–3086, Apr 1988.

[42] M. J. Lee. *Statistical modeling of wave chaotic transport and tunneling*. PhD thesis, University of Maryland, College Park, 2013.

[43] Wikipedia. Electromagnetic reverberation chamber — Wikipedia, the free encyclopedia. `https://en.wikipedia.org/wiki/Electromagnetic_reverberation_chamber`, 2017. [Online; accessed 23-October-2017].

[44] A. K. Fall, P. Besnier, C. Lemoine, M. Zhadobov, and R. Sauleau. Determining the lowest usable frequency of a frequency-stirred reverberation chamber using modal density. In *2014 International Symposium on Electromagnetic Compatibility*, pages 263–268, Sept 2014.

[45] IEC 61000-4-21:2011. Electromagnetic compatibility (EMC) - Part 4-21: Testing and measurement techniques - Reverberation chamber test methods. Standard, International Electrotechnical Commission, January 2011.

[46] Sameer Hemmady, James Hart, Xing Zheng, Thomas M. Antonsen, Edward Ott, and Steven M. Anlage. Experimental test of universal conductance fluctuations by means of wave-chaotic microwave cavities. *Phys. Rev. B*, 74:195326, Nov 2006.

[47] S. Pfennig and H. G. Krauthuser. A general method for determining the number of independent stirrer positions in reverberation chambers. In *International Symposium on Electromagnetic Compatibility - EMC EUROPE*, pages 1–6, Sept 2012.

[48] Louis M. Pecora, Hoshik Lee, Dong-Ho Wu, Thomas Antonsen, Ming-Jer Lee, and Edward Ott. Chaos regularization of quantum tunneling rates. *Phys. Rev. E*, 83:065201, Jun 2011.

[49] Ming-Jer Lee, Thomas M. Antonsen, Edward Ott, and Louis M. Pecora. Theory of chaos regularization of tunneling in chaotic quantum dots. *Phys. Rev. E*, 86:056212, Nov 2012.

[50] R. Owen and J. Rodgers. Electromagnetic cavities as an analog to chaos regularization of quantum tunneling rates. In *APS March Meeting Abstracts*, March 2015.

[51] Matthew Reagor, Hanhee Paik, Gianluigi Catelani, Luyan Sun, Christopher Axline, Eric Holland, Ioan M. Pop, Nicholas A. Masluk, Teresa Brecht, Luigi Frunzio, and et al. Reaching 10ms single photon lifetimes for superconducting aluminum cavities. *Applied Physics Letters*, 102(19):192604, 2013.

[52] MATLAB. *version 9.2 (R2017a)*. The MathWorks Inc., Natick, Massachusetts, 2017.

[53] Jen-Hao Yeh. *Wave Chaotic Experiments and Models for Complicated Wave Scattering Systems*. PhD thesis, University of Maryland, College Park, 2013.

[54] James Aamodt. Hart. *Scattering from chaotic cavities: exploring the random coupling model in the time and frequency domains*. PhD thesis, 2009.